

# Large scale and linear scaling DFT with the CONQUEST code

Ayako Nakata, Sergiu Arapan,<sup>\*</sup> Jianbo Lin, Zamaan Raza,<sup>†</sup> Sushma Yadav, and Tsuyoshi Miyazaki<sup>‡</sup>  
*International Centre for Materials Nanoarchitectonics (MANA),  
 National Institute for Materials Science (NIMS), 1-1 Namiki, Tsukuba, Ibaraki 305-0044, Japan*

Jack S. Baker, Shereif Y. Mujahed, and Jack T. L. Poulton  
*London Centre for Nanotechnology, University College London,  
 17-19 Gordon St, London, WC1H 0AH, UK and  
 Department of Physics & Astronomy, University College London, Gower St, London, WC1E 6BT, UK*

Lionel Truflandier  
*Institut des Sciences Moléculaires, Université Bordeaux,  
 351 Cours de la Libération, 33405 Talence, France*

David R. Bowler<sup>§</sup>  
*International Centre for Materials Nanoarchitectonics (MANA),  
 National Institute for Materials Science (NIMS), 1-1 Namiki, Tsukuba, Ibaraki 305-0044, Japan  
 London Centre for Nanotechnology, University College London,  
 17-19 Gordon St, London, WC1H 0AH, UK and  
 Department of Physics & Astronomy, University College London, Gower St, London, WC1E 6BT, UK  
 (Dated: January 27, 2022)*

We survey the underlying theory behind the large-scale and linear scaling DFT code, CONQUEST, which shows excellent parallel scaling and can be applied to thousands of atoms with diagonalisation, and millions of atoms with linear scaling. We give details of the representation of the density matrix and the approach to finding the electronic ground state, and discuss the implementation of molecular dynamics with linear scaling. We give an overview of the performance of the code, focussing in particular on the parallel scaling, and provide examples of recent developments and applications.

## I. INTRODUCTION

As computing power has increased and methods have become more sophisticated, so computational modelling of materials systems has taken its place alongside experiment and theory in science. Electronic structure methods give insight into bonding and electronic properties of systems, and density functional theory (DFT) is now the *de facto* method used in fields as diverse as physics, chemistry, earth sciences, materials science and biochemistry[1].

However, almost all DFT calculations are focussed on a relatively small system size, of a few hundred atoms (while feasible, calculations involving more than a thousand atoms are still considered expensive). This size limitation mainly comes from the cost and scaling of standard DFT implementations (asymptotically, the computer time required scales with the cube of the number of atoms in the system, while the memory scales with the

square of the number of atoms).

The use of increasingly large numbers of computational cores is one route to larger scale DFT calculations. Indeed, high-performance computing centres have recently scaled to tens of thousands and hundreds of thousands of cores, and exascale computing is scheduled to arrive in the next few years. However, efficient use of systems of this size requires care to ensure that the parallel scaling of any given code remains efficient as the number of cores becomes large. A real-space formulation, and the use of local basis functions to represent the Kohn-Sham (KS) eigenstates, can help with the parallel efficiency of the code, and enables calculations on larger systems, often with several thousand atoms[2–10]. Moreover, there is no inherent reason why DFT implementations should scale with the cube of the system size[11]; in fact, with local basis functions, DFT can be formulated in a linear scaling approach[12, 13].

The use of a few hundred atoms in a calculation potentially introduces many approximations, and in some cases errors. There are systems where larger scale calculations are necessary to model the properties correctly. Features with dimensions of nanometres or more, or features with strain fields over nanometres, will be seriously restricted by a small calculation as the strain will not be fully relaxed. Dilute alloys can change their properties if the concentration is incorrect (for instance the metal-insulator transition in doped silicon occurs at around  $2 \times 10^{19}$  dopants per cubic centimetre, or one dopant

<sup>\*</sup>Present address: IT4Innovations, VŠB - Technical University of Ostrava, 17. listopadu 2172/15, 70800 Ostrava-Poruba, Czech Republic

<sup>†</sup>Present address: Jlich Centre for Neutron Science (JCNS) at Heinz Maier-Leibnitz Zentrum (MLZ), Lichtenbergstrae 1, 85748 Garching, Germany

<sup>‡</sup>Electronic address: MIYAZAKI.Tsuyoshi@nims.go.jp

<sup>§</sup>Electronic address: david.bowler@ucl.ac.uk

per 50,000 silicon atoms). Calculations on biomolecules often use a small quantum mechanical (QM) region embedded into a larger forcefield (or molecular mechanics, MM) region, and it has been shown[14] that the size and choice of the QM region affects the results strongly, with sizes of at least 500 atoms being required. While there are accurate forcefields available, and new approaches to the fitting of forcefields are being developed, simulations requiring electronic structure or bond making and breaking must use DFT or a related approach.

CONQUEST is a large-scale and linear scaling DFT code which is designed to scale efficiently in parallel, and to be applicable to systems with thousands of atoms with full diagonalisation for the ground state, and to systems with millions of atoms with a linear scaling solution of the ground state. It has recently been released under an open-source MIT licence[15], and in this paper we describe the implementation of the code and various recent applications. We first describe the approaches to representing the density matrix, and finding the electronic ground state, and then consider how to eigenvectors can be calculated for systems large enough to require linear scaling. We also discuss the calculation of exact exchange with linear scaling. We then turn to the movement of atoms, considering in particular the calculation of stress, and the implementation of molecular dynamics, both with reference to linear scaling. After presenting the performance of CONQUEST for various systems, we then illustrate several applications with many thousands of atoms, before concluding.

## II. METHODS: ELECTRONIC STRUCTURE

### A. Pseudopotentials and pseudo-atomic orbitals

The default pseudopotential format used in CONQUEST is the optimised norm-conserving Vanderbilt pseudopotential (ONCVPSP) developed by Hamann[16] from Vanderbilt’s approach[17]. This approach has been used to generate two libraries covering most of the periodic table: PseudoDojo[18] and SG15[19]. Both of these libraries give very good values using the Delta comparison to all-electron results[20], with PseudoDojo showing an accuracy comparable to the best PAW (projector augmented waves) results (when using a fully-converged plane wave basis set).

This approach to pseudopotential generation is focussed on accuracy, and as a consequence includes semi-core states for many elements beyond the third row of the periodic table, as well as partial core corrections[21] in many cases. The spacing of the real-space integration grid required for these pseudopotentials may be finer than other approaches would give. CONQUEST is also compatible with pseudopotentials in the Troullier-Martins form as generated by SIESTA, which are less stringent, and thus less expensive.

As is common for local orbital approaches, we use a

neutral atom approach[22], where the local part of the pseudopotential and a (neutral) atomic density cancel each other out at large distances from the atom; among other things, this removes the need for an Ewald sum for the ion-ion energies. However, it has been shown[23] that the resulting potential can be deep, and require a fine integration grid for convergence. To alleviate this problem, we have implemented the neutral atom projector approach[23], and will report detailed testing in a future publication.

CONQUEST can use pseudo-atomic orbitals (PAOs) as basis functions to represent the support functions (discussed in Sec. II B below), while the valence orbitals also serve to generate the atomic density. We generate the PAOs[24] by solving the Schrödinger equation for an isolated, confined atom with a pseudopotential. The basis sets are formed from valence orbitals (with a given number of functions, or zetas, for each angular momentum, each with its own confinement) and polarisation functions (typically with  $l_v + 1$  where  $l_v$  is the angular momentum of the highest occupied state, and a given, different number of functions to the valence states).

The confinement is equivalent to a hard wall, and can be applied either as a radial cutoff, or an energy shift for the orbital, which generates a different radius for each orbital. The default basis sets in CONQUEST are generated either with the same radial cutoffs for all shells, or the same energy shifts. For the energy shifts, we use a tight confinement (a shift of 2eV) and a loose confinement (a shift of 0.02 eV) to generate two zeta functions, with a third generated when needed using the average radius of the first two. The uniform radial confinement is found as the average of the radii for all valence functions with the large or small energy confinement, with the third radius again found as an average. Semi-core states only use one function with a loose confinement (in this case the orbital is strongly confined so that even a very small energy shift gives good results).

We have tested our default basis sets (single zeta with polarisation, SZP, double zeta with polarisation, DZP, and triple zeta with triple polarisation, TZTP) against converged plane wave calculations using the same pseudopotentials[24]. We used a wide variety of systems: elemental semiconductors (C, Si, Ge); oxides (SiO<sub>2</sub> in both  $\alpha$ -quartz and stishovite phases, MgO, SrTiO<sub>3</sub>, PbTiO<sub>3</sub> and MgSiO<sub>3</sub>); non-magnetic bcc Fe; and weakly bonded systems (ice XI and BN sheets). In all cases, we showed that the TZTP basis sets reproduced the converged plane wave results with excellent accuracy: better than 1% in bulk modulus and 0.1% of the lattice constant, for a variety of bulk systems; full details are found in Ref. 24.

### B. Representing the density matrix

CONQUEST uses the density matrix as the fundamental description of the system being modelling (in contrast to

the wavefunctions as is common in many DFT codes). The density matrix is represented in terms of support functions[25, 26],  $\phi_{i\alpha}(\mathbf{r})$ , where  $i$  indexes the atom and  $\alpha$  the function on the atom, and can be written:

$$\rho(\mathbf{r}, \mathbf{r}') = \sum_{i\alpha, j\beta} \phi_{i\alpha}(\mathbf{r}) K_{i\alpha, j\beta} \phi_{j\beta}(\mathbf{r}') \quad (1)$$

(Note that the density matrix can easily be written in terms of the wavefunctions, when these are available, or found by linear scaling optimisation, as described in Section II C. Note also that, while we assume a non-spin-polarised calculation here, the extension to spin polarisation is straight-forward and has been implemented in CONQUEST.)

The support functions are local functions which move with the atoms, and are strictly localised within a sphere. They are used to form the Hamiltonian and overlap matrices as well as to represent the density matrix:

$$H_{i\alpha, j\beta} = \int d\mathbf{r} \phi_{i\alpha}(\mathbf{r}) \hat{H} \phi_{j\beta}(\mathbf{r}) \quad (2)$$

The support functions themselves are defined either as primitive PAOs (in a one-to-one mapping), or are represented in terms of one of two basis sets: the PAOs; or blip functions[27]. We write:

$$\phi_{i\alpha}(\mathbf{r}) = \sum_s b_{i\alpha s} \theta_s(\mathbf{r}) \quad (3)$$

where the basis functions  $\theta_s(\mathbf{r})$  (either pseudo-atomic orbitals or cubic B-splines) are discussed further below.

### 1. Multi-site support functions

Since the primitive PAOs are localized around the atoms, we can use them as support functions without any modifications, and a large PAO basis set gives high accuracy, as shown in Sec. II A. However, the computational cost of calculations scales with the cube of the number of support functions. For large-scale calculations, we need to reduce the number of support functions as much as possible. We note that there is a strong link between the basis set chosen and the number of support functions that can be used[28].

Multi-site support functions (MSSF)[29, 30] offer one way to reduce the number of support functions. The MSSF are constructed as linear combinations of the PAOs not only on the target atom, but also on its neighbouring atoms, defined by a cutoff radius  $r_{\text{MS}}$ ,

$$\phi_{i\alpha}(\mathbf{r}) = \sum_k^{i, \text{neighbours}} \sum_{\mu \in k} C_{i\alpha, k\mu} \chi_{k\mu}(\mathbf{r}), \quad (4)$$

where  $\chi_{k\mu}$  is a PAO on atom  $k$ ,  $\alpha$  is the index of the support functions of atom  $i$ ,  $\mu$  is the index of the PAOs of

its neighbouring atoms  $k$  (including  $i$  itself), and  $C_{i\alpha, k\mu}$  are the linear combination coefficients. Since the MSSF are no longer atomic orbitals but local molecular orbital (MO)-like functions, the number of MSSF can be equal to that of a minimal basis.

In CONQUEST, two methods have been implemented to determine the linear-combination coefficients of the MSSF. One of the methods is the local-filter-diagonalisation (LFD) method proposed by Rayson and Briddon [5, 29, 31], and the other is numerical optimisation[30], which will be explained in Sec. II C. In the LFD method, as shown in Eq. 5, the coefficients  $\mathbf{C}$  for each atom are found by diagonalising a subspace Hamiltonian matrix defined by a cluster of radius  $r_{\text{LFD}}$  centred on the atom, constructed with PAOs; the coefficients,  $\mathbf{C}_{\text{sub}}$ , for the resulting eigenstates, or local molecular orbitals, are projected onto trial support functions,  $\mathbf{t}$ , localised on the target atom:

$$\mathbf{C} = \mathbf{C}_{\text{sub}} f(\epsilon_{\text{sub}}) \mathbf{C}_{\text{sub}}^T \mathbf{S}_{\text{sub}} \mathbf{t}, \quad (5)$$

where  $\mathbf{S}_{\text{sub}}$  is the overlap matrix and  $f(\epsilon_{\text{sub}})$  is a Fermi function with a local Fermi level  $\epsilon_{\text{sub}}$ , used to exclude high energy unoccupied local molecular orbitals. Since the MSSF will depend on the charge density of the system, which will in turn depend on the MSSF, the linear-combination coefficients need to be determined self-consistently [29].  $r_{\text{MS}}$  should be equal to or smaller than the subspace region in the LFD method  $r_{\text{LFD}}$ .

The accuracy of the MSSF depends on  $r_{\text{MS}}$ . In Fig. 1, we see that the deviation from the full, unrestricted, primitive PAO result decreases exponentially not only in a gapped system (bulk Si) but also in a metallic system (bulk Al). The number of MSSF per atom is four, while that of the TZP PAOs is 17 in both Si and Al, giving a four-fold reduction in number and a significant speed-up. An example of the computational time with the MSSF is demonstrated in Sec. IV A.

### 2. On-site support functions

When using a linear scaling solver, as described in Sec. II C, we require a sparse approximation to the inverse overlap matrix to act as a metric[32]. We have found that multiple zeta basis sets, and multi-site support functions, are not compatible with our standard linear-scaling method for finding this inverse overlap (Hotelling's method). The reasons for this failure are not yet clear, and are under investigation, but are most likely to arise from the assumed sparsity pattern of the matrix, and the starting value used[127]. As a result, we have been limited in the basis sets that can be used for linear scaling. Blip functions, which will be discussed in Sec. II B 3, offer an route to an accurate linear scaling basis set; however, PAOs are often convenient and efficient, and a restriction to SZ or SZP PAO basis sets is limiting.

We have found recently, however, that an adaptation of the MSSF approach allows linear scaling solution for

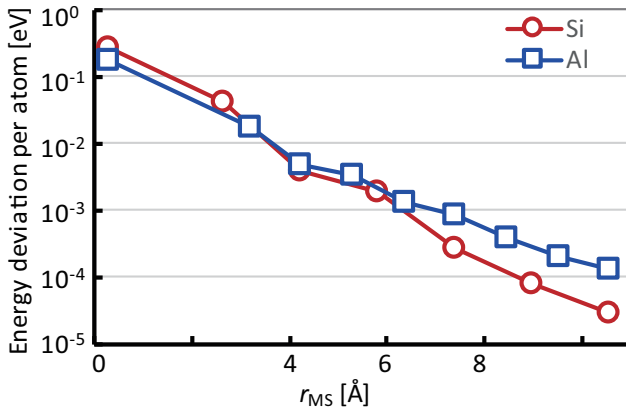


FIG. 1: Difference of total energy per atom [eV] with MSSF from the full primitive PAO result, with respect to the multi-site range  $r_{\text{MS}}$ . The local diagonalization range  $r_{\text{LFD}}$  was set to be equal to  $r_{\text{MS}}$ . The circles and squares correspond to bulk Si and Al. (Data taken from J. Chem. Theory Comput. 10, 4813 (2014) with permission. Copyright (2014) American Chemical Society.)

a sparse inverse overlap matrix while retaining accurate basis sets: on-site support functions (OSSF). We restrict the PAOs forming the support functions for an atom  $i$  to its own PAOs; however, we must be careful to respect any symmetry of the atomic lattice, so that the space spanned by the support functions of the atoms decomposes into complete irreducible representations of the symmetry group[28]. The simplest way to ensure that this is respected is to increase the number of support functions such that it encompasses all angular momenta of the PAOs (e.g. for PAOs including  $l = 0 \rightarrow 2$  we would need 9 SFs, while for PAOs only including  $l = 0$  and  $l = 2$  we would need 6 SFs).

This approach bears some similarity to the polarised atomic orbital method[33, 34] though that method imposes no restrictions on the number of functions, and uses a different approach to find the orbital coefficients. In our approach we use the LFD method described in Sec. II B 1, using a trial vector which is extended to include the polarisation orbitals. We find that the resulting support functions can be inverted efficiently (interestingly, it is often more efficient than a simple SZP PAO basis set).

When using OSSF with linear scaling, we are still investigating the most efficient approach for finding the ground state; this involves optimising the density matrix, the OSSF coefficients and the charge density. Introducing self-consistency between the OSSF coefficients and the charge density is straightforward, but in a naive loop would add considerably to the computational time. Optimising the energy with respect to the OSSF coefficients is also straightforward, but the most efficient approach (i.e. when to update which parts of the optimisation)

requires further research.

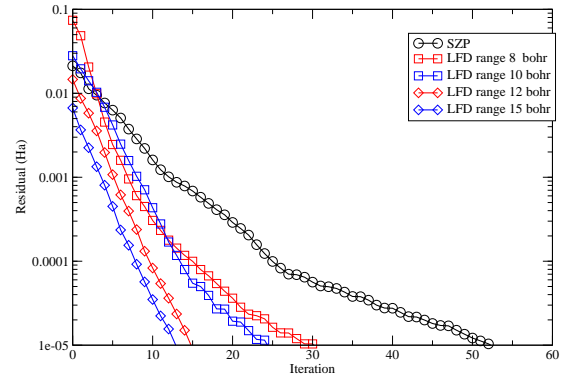


FIG. 2: Convergence of linear scaling density matrix optimisation for different basis sets: SZP; and OSSF with different LFD ranges. The system considered is an eight atom bulk silicon cell, slightly disturbed from the perfect crystal structure.

The basis sets found using OSSF are significantly better than the simple SZP PAO basis set, as shown in Fig. 2. Here we see that, for a slightly disturbed eight atom bulk silicon cell, as the LFD range is progressively increased, so the rate of convergence of the density matrix optimisation improves. The quality of the resulting approximate inverse overlap matrix is also improved, and the energy and forces on the atoms are significantly better with the OSSF basis sets. We show results for different basis sets in Table I: primitive PAOs (SZP, DZP and TZTP); MSSF for different ranges; and OSSF. The MSSF and OSSF calculations do not update the SF coefficients after finding self-consistency; for MSSF, the LFD range is set to 15 bohr throughout. Note that the energy is not variational with respect to the radius in this simple process, though with optimisation (as described in Sec. II C 3) it will be variational.

As seen in Fig. 2, it is evident that the OSSF give a significant improvement to the performance of the linear scaling solver, and from Table I we can see that they are comparable to the MSSF for the accuracy of forces and the timing. Most notably, we see that with the OSSF found with the LFD radius set to 15 bohr, the linear scaling solver is only 2 times slower than diagonalisation with the full TZTP basis set, and 8 times slower than the DZP basis set. This performance difference is expected for such a small system where linear scaling solvers are less efficient than diagonalisation and related solvers. However, it suggests that the choice of basis functions is important in implementing linear scaling. We note that the quality of both OSSF and MSSF basis sets would be improved by optimisation of the coefficients, as described in Sec. II C 3, but even with these simple approximations, good performance is achieved.

Basis	Energy (Ha)	Force (Ha/bohr)	Time relative to TZTP
SZP	-33.714	-0.00170	0.12
DZP	-33.819	-0.00151	0.23
TZTP	-33.838	-0.00145	1.00
MSSF 5 bohr	-33.800	-0.00154	0.68
MSSF 8 bohr	-33.821	-0.00143	0.73
MSSF 10 bohr	-33.818	-0.00143	0.73
MSSF 12 bohr	-33.828	-0.00144	0.81
OSSF 8 bohr	-33.625	-0.00162	0.63
OSSF 10 bohr	-33.813	-0.00142	0.63
OSSF 12 bohr	-33.812	-0.00142	0.60
OSSF 15 bohr	-33.820	-0.00142	0.86
OSSF $\mathcal{O}(N)$ 8 bohr	-33.605	-0.00174	4.20
OSSF $\mathcal{O}(N)$ 10 bohr	-33.784	-0.00154	3.68
OSSF $\mathcal{O}(N)$ 12 bohr	-33.782	-0.00154	2.87
OSSF $\mathcal{O}(N)$ 15 bohr	-33.792	-0.00154	2.47

TABLE I: Comparison of different basis sets for an eight atom bulk silicon cell, slightly disturbed from the perfect crystal structure. Primitive basis sets have 9, 13 and 27 support functions, respectively; MSSF have 4 support functions and a LFD range of 15 bohr; OSSF have 9 support functions. MSSF and OSSF are not updated after the initial calculation of the coefficients. The range on the density matrix for the  $\mathcal{O}(N)$  calculations was 16 bohr.

### 3. Blip functions

While PAOs are a convenient basis set, they do not permit systematic convergence of the energy with respect to the basis: while adding extra basis functions will increase the size of the variational space and lower the energy, there are two parameters which offer different degrees of freedom (maximum angular momentum, and number of radial functions, or zetas, per angular momentum channel), and there are no guarantees of how adding to each parameter will change the energy.

The blip functions[27], which are piecewise continuous cubic splines defined on a cubic grid that moves with the atoms, are a basis set that can be systematically converged. The blip grid spacing corresponds directly to a plane wave cutoff, allowing the basis set to be improved systematically (of course, the support functions are confined within a radius, but it has been shown that the total energy converges variationally and rapidly with this radius[27, 35]). The most efficient procedure for initialisation and optimisation of the blip coefficients along with the charge density, and for linear scaling approaches to finding the density matrix, is the subject of on-going research.

### C. Solving for the ground state

The ground state electronic structure in CONQUEST is defined by three related quantities: the support functions; the density matrix; and self-consistency between the charge density and the Kohn-Sham potential. The self-consistency procedure is a standard part of DFT and related codes[36], and we implement the Pulay approach[37] which works efficiently.

While the overall search for the ground state could be considered as an optimisation in a space formed by both the support function coefficients and the density matrix elements, it is easier to consider how the density matrix is found for a given set of support functions, and then to discuss methods for optimising the energy with respect to the support function coefficients. We consider first the two approaches to solving for the density matrix: exact diagonalisation[128], which scales cubically but makes no approximations; and linear scaling, which imposes a range on the density matrix.

#### 1. Density matrix: exact diagonalisation

We perform diagonalisation of the Hamiltonian using ScaLAPACK[38], and are also investigating the use of ELPA[39] (which uses the same interface, and may scale better to large numbers of processes).

Since we apply periodic boundary conditions to our simulation cell, the Brillouin zone must be sampled appropriately; we have implemented the Monkhorst-Pack[40] sampling method as a default approach to Brillouin

zone sampling, but any arbitrary set of k-points can be used. (At present we do not account for the symmetry of the simulation cell beyond time-reversal symmetry, as the code is designed for large-scale simulations which are unlikely to show significant symmetries.)

The Kohn-Sham eigenstates are represented in terms of the support functions, with the density matrix found as:

$$|\psi_{n\mathbf{k}}\rangle = \sum_{i\alpha} c_{i\alpha}^{n\mathbf{k}} |\phi_{i\alpha}\rangle \quad (6)$$

$$K_{i\alpha,j\beta} = \sum_{n\mathbf{k}} f_{n\mathbf{k}} w_{\mathbf{k}} c_{i\alpha}^{n\mathbf{k}} (c_{j\beta}^{n\mathbf{k}})^* \quad (7)$$

where the weight of each k-point is given as  $w_{\mathbf{k}}$  and the occupancy of the eigenstate is  $f_{n\mathbf{k}}$  (which is found using a simple Fermi-Dirac distribution, or the Methfessel-Paxton[41] approach). The diagonalisation at each k-point can be assigned to a sub-group of processes, enabling a calculation using many k-points to be sped up significantly.

#### 2. Density matrix: linear scaling

To achieve linear scaling in computational time with the system size, we restrict the range of the density matrix (the range of a matrix  $A_{i\alpha,j\beta} = 0$  is defined in terms of the distance between atoms  $i$  and  $j$ ,  $R_{ij} = |\mathbf{R}_i - \mathbf{R}_j|$ , and is restricted by setting matrix elements to zero when  $R_{ij}$  is greater than a cutoff distance  $R_c$ ), and optimise the band energy,  $E_{\text{band}} = 2\text{Tr}[KH]$ , with respect to the density matrix elements. When this approach is coupled with strictly local basis functions, all matrices are sparse, and all matrix operations scale linearly with system size.

During the optimisation, we must constrain the electron number (a relatively straightforward task[25]), and also the idempotency of the density matrix (a much more complex task in a variational context). We follow the LNV (Li, Nunes and Vanderbilt) approach[42, 43] where we write the density matrix  $K$  in terms of an *auxiliary* density matrix  $L$ , using the McWeeny transform:

$$K = 3LSL - 2LSLSL \quad (8)$$

This drives the density matrix,  $K$ , towards idempotency (strictly it is driven towards *weak* idempotency, where the eigenvalues lie between zero and one, but may not be exactly zero and one). If, as above, we write  $E = \text{Tr}[KH]$  then we can use the gradient  $\partial E / \partial L_{i\alpha,j\beta}$  to minimise the energy with respect to the density matrix, and the density matrix  $K$  will be driven towards idempotency as the minimisation proceeds. Here the range of  $K$  is the same as the range of the Hamiltonian (which is naturally sparse); it is  $L$  whose range is restricted, and this range sets the accuracy of the calculation.

The initial density matrix is generated from the Hamiltonian, using an iterative procedure based on a generalisation of the McWeeny transform[44, 45]. We use an

$r_{\text{MS}}$	$a_0$		%D	
	LFD	opt	LFD	opt
5.0	5.447	5.406	1.0	0.2
8.0	5.403	5.400	0.2	0.1
17.0	5.393	5.395	0.0	0.0
TZDP	5.395		—	

TABLE II: Lattice constants  $a_0$  of bulk Si calculated with MSSF with ranges  $r_{\text{MS}}$  of 5.0, 8.0 and 17.0 bohr, and percent deviations (%D) from  $a_0$  calculated with the primitive TZDP PAOs.

approximate, sparse inverse overlap matrix as the metric for the optimisation, found using the iterative Hotelling method. As discussed in Sec. II B, this has certain consequences for the basis sets that can be used, but both OSSF and blip basis sets show promise for accurate, linear scaling calculations.

### 3. Optimising support functions

As mentioned in Sec. II B, we can construct support functions by taking linear combinations of PAOs (MSSFs or OSSFs) or blips. The linear combination coefficients can be optimised numerically by minimizing the DFT total energy with respect to the coefficients[30]. For MSSFs and OSSFs, the coefficients obtained by the LFD method generally form good initial values for the numerical optimisation. The initial blip coefficients are found as a best fit to PAOs. In this section, we demonstrate optimisation of SF coefficients for the MSSFs, though the formalism is identical for the other approaches. We note that these optimisation processes are liable to ill-conditioning, which can be mitigated[46].

Figure 3 shows the energy-volume (E-V) curves of bulk Si[30] calculated with simple LFD (filled symbols) and optimisation of the MSSF coefficients (open symbols). The number of MSSFs per atom is four, while that of the primitive TZDP (3s3p2d) PAOs is 22. Table II summarises the lattice constant  $a_0$  obtained by fitting the E-V curves with the Birch-Murnaghan equation. The results are improved, i.e., becoming closer to the results of the primitive PAOs, by the numerical optimisation in all cases. When  $r_{\text{MS}}$  is large, e.g. 17.0 bohr, since the MSSFs found with LFD give accurate results, the change from numerical optimisation is small. When  $r_{\text{MS}}$  is 8.0 bohr, the difference with and without the numerical optimisation is significantly larger, but both LFD and the numerical optimisation show reasonable accuracy. On the other hand, when  $r_{\text{MS}}$  is as small as 5.0 bohr, the result with the LFD method is not accurate, with a 1% deviation from the full TZDP result, but we find significant improvement of the accuracy from numerical optimisation, reducing the percentage deviation to 0.2%.

## D. Electronic structure for large systems

Linear scaling, or  $\mathcal{O}(N)$ , calculations which work with the density matrix implicitly integrate over energy and produce only the sum of the occupied eigenvalues and not any of the Kohn-Sham eigenstates of the system. However, we often want to know individual eigenstates to analyze the electronic structure of the system, though generally within a relatively small energy range. These can be found efficiently from the converged ground-state Hamiltonian by using the Sakurai-Sugiura (SS) method[47]. The SS method [48, 49] is an efficient interior eigenproblem solver for large sparse matrices using contour integrals in the complex plane, which provides the eigenvalues and eigenvectors in a finite eigenvalue range with high parallel efficiency. We use the SS method as it is much more scalable in parallel than other approaches such as shift-and-invert Lanczos[50].) We first optimise the electronic Hamiltonian with the  $\mathcal{O}(N)$  method in CONQUEST, and then obtain the eigenstates of the Hamiltonian in a finite energy window with a one-shot SS calculation. Here we demonstrate the usefulness of the combination of the  $\mathcal{O}(N)$  and SS methods by showing two examples.

The first example is the energy-specific electron-density distribution in a hut-shaped Ge cluster on Si(001) surface consisting of 23,737 atoms (the physical system is described in more detail in Sec. V A). Figure 4 shows the electron density distribution in the energy range [-0.01 eV: + 0.02 eV] around the Fermi level, obtained by calculating the Kohn-Sham eigenvectors in this range with the SS method. The calculation for the eigenvalues and eigenvectors required 146 seconds using 64 nodes of the K supercomputer. We also calculated the eigenstates in the same energy range for a larger Ge/Si(001) system, consisting of 194,573 atoms, in 2,399 seconds using 6,400 nodes. (Note that the times quoted are just for the SS eigensolutions, which are performed as post-processing calculations using output from CONQUEST).

The second example is the density of states (DOS) of a DNA system in water, which consists of 3,439 atoms. The DOS calculated with MSSF (see Sec. II B 1) (4,774 functions) and primitive PAOs (27,883 functions), and their difference are shown in Fig. 5. The DOS from the MSSF is very close to the full primitive PAO DOS in the occupied states, and in the unoccupied states near the Fermi level, while the DOS in the unoccupied states far from Fermi level are quite different. This is because the MSSFs are determined by optimising the occupied states with a small number of support functions, and the accuracy of the MSSFs for unoccupied states often becomes poor. To improve this poor description, we can use the SS method. First, we optimise the electronic density of the target system using MSSF, and we re-construct the electronic Hamiltonian using the primitive PAOs with the optimised density. Then we use the SS method to obtain the eigenstates. Thus, we can obtain the DOS even in unoccupied states far from Fermi level quite accurately,

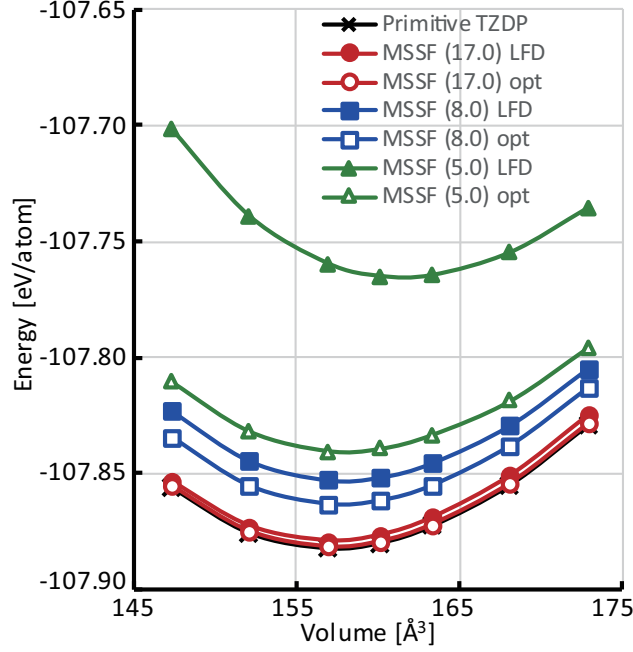


FIG. 3: Energy-volume curves of bulk Si, demonstrating the effect of optimising MSSF coefficients after the initial LFD process. Symbols correspond to the calculated energies by primitive TZDP PAOs and MSSF with multi-site ranges ( $r_{\text{MS}}$ ) 17.0, 8.0 and 5.0 bohr, using the LFD method (filled symbols) and numerical optimisation (open symbols). The local filter diagonalization range  $r_{\text{LFD}}$  was set to be equal to  $r_{\text{MS}}$ . (Adapted from Ref. 30 with permission from the PCCP Owner Societies.)

as shown in Fig. 5.

### E. Exact exchange

Exact exchange (EXX) correction to the original Kohn-Sham formulation of DFT, leading to the class of

*hybrid* exchange-correlation functionals, has become very popular, since in the vast majority of cases, it improves the overall reliability of the DFT predictions. Depending on the implementation — mainly basis set and boundary conditions — orbital dependence is introduced to the KS-DFT formalism *via* the EXX energy standard expression:

$$E_x = -\frac{1}{4} \int d\mathbf{r} d\mathbf{r}' \frac{\rho(\mathbf{r}, \mathbf{r}') \rho(\mathbf{r}', \mathbf{r})}{|\mathbf{r} - \mathbf{r}'|} = -\sum_{n,m} \int d\mathbf{r} d\mathbf{r}' \frac{\psi_n^*(\mathbf{r}) \psi_m^*(\mathbf{r}') \psi_n(\mathbf{r}) \psi_m(\mathbf{r}')}{|\mathbf{r} - \mathbf{r}'|}, \quad (9)$$

where  $\{\psi_n\}$  is the set of  $N$  occupied KS states, can bring the computational cost to a prohibitive level more rapidly than pure LDA/GGA DFT when increasing the system size. Within the framework of CONQUEST, where the

density matrix of Eq. 9 are expanded onto a set of  $M$  localized and real basis functions, the exchange energy reads:  $E_x = -\text{Tr}\{KX\}$ , with the exchange matrix ( $X$ ) elements given by:

$$X_{i\alpha,j\beta} = \sum_{k\mu,l\nu} \int d\mathbf{r} d\mathbf{r}' \frac{\phi_{i\alpha}(\mathbf{r}) \phi_{k\mu}(\mathbf{r}) K_{k\mu,l\nu} \phi_{l\nu}(\mathbf{r}') \phi_{j\beta}(\mathbf{r}')}{|\mathbf{r} - \mathbf{r}'|} = \sum_{k\mu,l\nu} \int d\mathbf{r} d\mathbf{r}' \frac{\phi_{i\alpha}(\mathbf{r}) \phi_{k\mu}(\mathbf{r}) K_{k\mu,l\nu} \phi_{l\nu}(\mathbf{r}') \phi_{j\beta}(\mathbf{r}')}{|\mathbf{r} - \mathbf{r}'|}. \quad (10)$$

As a result, calculation of  $X$  requires to evaluate at most

$M^4$  electron repulsion integrals (ERIs) defined by the



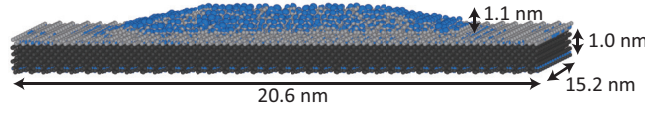


FIG. 4: Electronic density distributions (blue) of the Ge hut clusters (light gray) on the Si(001) (dark gray) (totally 23,737 atoms) around the Fermi level. (Reprinted with permission from J. Chem. Theory Comput. 13, 4146 (2017). Copyright (2017) American Chemical Society.)

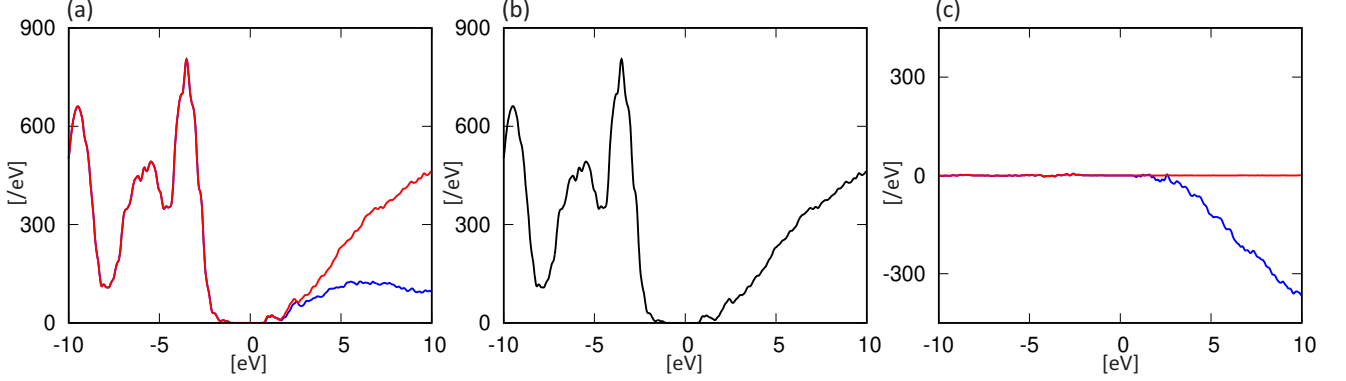


FIG. 5: Density of states of hydrated DNA obtained with (a) multi-site support functions (MSSF) with multi-site range 8.0 bohr (blue) and DZP PAOs using MSSF charge density (red) and (b) DZP PAOs using DZP SCF charge density (black). The difference of (a) MSSF (blue) and DZP with the MSSF density (red) from (b) DZP is also shown in (c). The eigenstates in (a) and (b) were obtained by the SS method. (Reprinted with permission from J. Chem. Theory Comput. 13, 4146 (2017). Copyright (2017) American Chemical Society.)

integrand of Eq. 10. The first equality in the equation above outlines the fact that evaluating an ERI is similar to computing the Hartree energy, with in place of the full electronic density, localized pair densities ( $\rho_{i\alpha,k\mu}, \rho_{l\nu,j\beta}$ ) coupled by the density matrix elements  $K_{k\mu,l\nu}$ . Consequently, ERI calculation can be performed by solving a Poisson equation into a predefined local cell. Note that, contrary to the Hartree energy, solution of this equation should be free of periodic boundary conditions.

When dealing with a numerical basis set such as the PAOs, several options to compute the ERIs are available, with for instance the semi-analytic solution given by Toyoda and Ozaki[51, 52] combining fast-spherical Bessel transform for the radial integration and a more traditional analytic method for the spherical harmonic part. Another approach is based on the experience of Gaussian-type orbital (GTO) ERI solvers.[53] In that case, the PAO-ERIs are transformed into a set of contracted GTO-ERIs which are then calculated analytically.[54, 55] Instead, we use a route which circumvents the calculation of the ERIs and works for any smooth finite-range functions, which is particularly well suited for  $\mathcal{O}(N)$  approaches based on the pseudopotential approximation. The key part is to perform the sum over the index  $l\nu$  before solving for the Coulomb potential of the pair densities; this simple re-ordering increases the efficiency of the procedure markedly. For this, we introduce the con-

traction functions,  $\Phi_{k\mu}(\mathbf{r}')$ , as:

$$\Phi_{k\mu}(\mathbf{r}') = \sum_{l\nu} K_{k\mu,l\nu} \phi_{l\nu}(\mathbf{r}') \quad (11)$$

It should be noted that the domain over which these functions are defined requires some care.[56] The sum over  $l\nu$  need only include those support functions  $\phi_{l\nu}$  overlapping with  $\phi_{j\beta}$ , as  $\Phi_{k\mu}$  will be multiplied by this function. Contracted densities are then defined as

$$\bar{\rho}_{k\mu,j\beta}(\mathbf{r}') = \Phi_{k\mu}(\mathbf{r}') \phi_{j\beta}(\mathbf{r}'), \quad (12)$$

and the resulting Coulomb potential,

$$\bar{v}_{k\mu,j\beta}(\mathbf{r}) = \int d\mathbf{r}' \frac{\bar{\rho}_{k\mu,j\beta}(\mathbf{r}')}{|\mathbf{r} - \mathbf{r}'|}, \quad (13)$$

is calculated by solving Poisson's equation. Once the potential has been found, a further contraction over  $k\mu$  is performed to create,

$$\Omega_{j\beta}(\mathbf{r}) = \sum_k \bar{v}_{k\mu,j\beta}(\mathbf{r}) \phi_{k\mu}(\mathbf{r}), \quad (14)$$

where, again, the sum over support functions  $k\mu$  need only include those functions which overlap with functions  $i\alpha$ . The exchange matrix elements are then calculated by numerical integration:

$$X_{i\alpha,j\beta} = \int d\mathbf{r} \phi_{i\alpha}(\mathbf{r}) \Omega_{j\beta}(\mathbf{r}). \quad (15)$$

The process —from Eq. 11 to (15)— by which the EXX is calculated in CONQUEST, will be referred as to the contraction reduction integral (CRI). The set of function  $\Omega_{j\beta}$  is effectively defined by the density matrix range, and the need for  $j\beta$  to overlap with atoms  $lv$ , which naturally control the number of functions entering in the sums of Eqs. (12) and (14). Note that the calculation time can be reduced by imposing a range condition ( $R_X$ ) on the exchange matrix. This is related to the sparsity property[11] of  $\rho(\mathbf{r}, \mathbf{r}')$  and the truncation of all the operators involved in the Hamiltonian.[25]

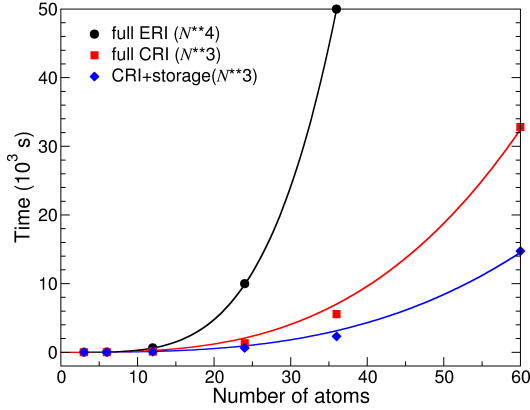


FIG. 6: Comparison of CPU times necessary to compute EXX in isolated water clusters as a function of number atoms ( $N$ ) using explicit ERI calculation and the CRI method. Ideal  $N^4$  and  $N^3$  scalings are given by plain lines.

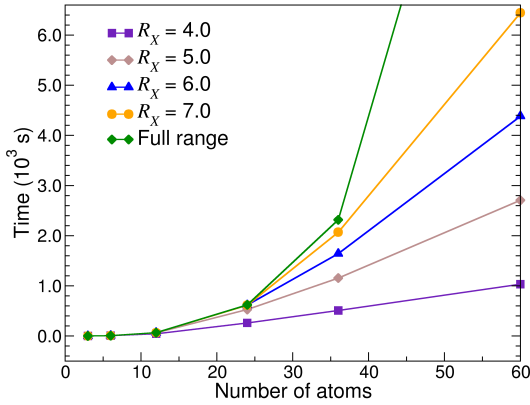


FIG. 7: Variation of the CPU time with respect to the range  $R_X$  (in a.u.) for the calculation of EXX in isolated water clusters using the CRI method.

Practical tests on the efficiency of this approach algorithm were carried out on a set of isolated water clusters  $(\text{H}_2\text{O})_n$  ( $n \leq 20$ ) with fused cubes structures.[57] Calculations of exchange energy were performed after the KS density matrix had been converged using the standard self-consistent-field (SCF) method. As a result, the

timings presented below for exact exchange (EXX) energy can be compared to a single SCF cycle as found in hybrid-DFT calculation. For this demonstration, SZP PAO orbitals have been used for hydrogen and oxygen with cutoff radii of 4.7 and 3.8 au, respectively. We emphasize that the main conclusions of this work can be easily extended to more flexible basis sets, as long as the support functions are localized. The CPU times used for the computation of EXX are reported in Fig. 6 as a function of the number of atoms using: (i) the explicit evaluation of the full set of ERI, (ii) the CRI approach, and (iii) the CRI approach with partial storage of the PAO on the grids. Comparing the formal scalings obtained for the CRI methods against the full ERI approach, it becomes clear that the former reduces the quartic scaling to cubic with respect to the size of the system.

At this point we should emphasise that exchange energy values obtained with the three schemes are fully identical, their accuracies being only dependent on the Poisson solver used to evaluate the pair potential in Eq. 13. Among the various numerical methods, one can choose to evaluate the Coulomb potential in reciprocal or real space. Whereas the former is the most appropriate for periodic neutral systems —when the positively charged nuclei compensate exactly the electronic charge density— it becomes less reliable for isolated and/or charged systems.[58] Several schemes have been developed to tackle this problem,[59–62] Alternatives based on the discrete variable representation (DVR) of Eq. 13 which avoids the direct resolution of the Poisson equation have been proposed.[63] The density is generally expanded in a direct product of one-dimensional localized real-space basis functions[63–65] as for instance, interpolating scaling functions (ISF). After extended comparisons between the DVR-ISF developed by Genovese et al.[66, 67] and corrected FFT-based schemes,[68–70] we found that systematic convergence of the ERI is obtained with a better accuracy and at a lower cost using the real space Poisson solver.

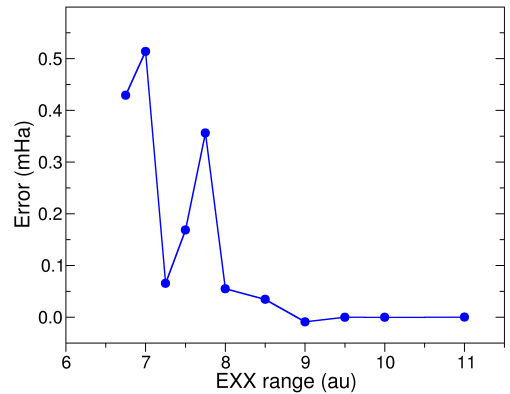


FIG. 8: Convergence of the EXX energy with respect to the exchange range  $R_X$  for the cluster  $(\text{H}_2\text{O})_{20}$ . Error is given with respect to the exact calculation.

As shown in Fig. 7, if a finite range  $R_X$  is introduced within the CRI algorithm, the CPU time can be significantly reduced, allowing linear scaling to be achieved for clusters with more than 36 atoms (with  $R_X = 7.0$  au). Computational resources further decrease with shorter EXX ranges, along with faster onset of the linear-scaling regime. The EXX accuracy with respect to the range of the exchange matrix is shown in Fig. 8 for the cluster  $(\text{H}_2\text{O})_{20}$  presenting the “boxkite” structure. After somewhat erratic behavior at low values, it is found that an accuracy below 0.5 mHa is reached for  $R_X \geq 8$ . Even though the non-local nature of the EXX interaction may need some special care when introducing a cutoff radius on  $X$  elements, it is reasonable to believe that the CRI implementation, along with a judicious choice of convergence parameters, is opening the way to exact exchange calculations on 100,000+ atoms with CONQUEST for a fair efficiency/accuracy ratio.

### III. METHODS: MOVING ATOMS

#### A. Forces and stresses

Forces have been available in CONQUEST for some time, as described elsewhere[71, 72], with the force being the exact differential of the energy, including Pulay forces where appropriate.

Calculation of the stress tensor has recently been implemented within the current release of CONQUEST. The definition of the stress tensor is standard[2]:

$$\sigma_{\alpha\beta} = \frac{\partial E}{\partial \epsilon_{\alpha\beta}} = \frac{\partial E}{\partial r_\alpha} r_\beta \quad (16)$$

where  $\alpha$  and  $\beta$  are Cartesian directions indices, and the second equality holds for *most* contributions to the stress. In this case, the first term is the force, so most contributions to the stress tensor can be calculated at the same time the forces are calculated. There are a few exceptions to this, however, but they are easily evaluated[2, 73].

The original formulation of stress within DFT is traced back to the pioneering work of Nielsen and Martin[74, 75], where a formulation for the stress was expressed for the first time in the framework of the local-density approximation (LDA) and later derived in more detail[76, 77]. We have chosen to omit the factor of  $\frac{1}{\Omega}$  in eq. 16 since it *averages* the total stress over the macroscopic simulation cell and in a case where the volume  $\Omega$  is not well defined would give spurious results. Note that *pressure*, as calculated at present, uses the volume of the simulation cell for the purpose of conversion and if there is vacuum in any direction the pressure should not be considered accurate. For this reason CONQUEST internally uses values of stress to optimise simulation cells.

Stress is an extremely useful quantity: it is used to optimise simulation cell parameters, though this requires care to converge both the integration grid spacing, and

numbers of k-points. Additionally, it is used in the NPT ensemble for molecular dynamics.

Our implementation of stress is valid for both exact diagonalisation and linear scaling solvers. However, we have found that the stress converges extremely slowly with respect to density matrix truncation. Figure 9 shows the convergence of force (i.e. energy differences), total energy and stress with density matrix truncation for three different elemental semiconductors with very different gaps: carbon, silicon and germanium. Calculations were performed on the diamond structure (with a small perturbation in the case of the force calculation) at the optimal lattice parameter found using exact diagonalisation, with integration grid spacing of 0.1 Bohr radii and an  $8 \times 8 \times 8$   $\Gamma$ -centred Monkhorst-Pack grid. To aid comparison between exact diagonalisation and linear scaling calculations, we used the simplest basis set, i.e. single zeta, though this does not change the final results significantly. The plots show the difference between the  $\mathcal{O}(N)$  and full diagonalisation results. The full diagonalisation results for the stresses were all less than 0.001Ha (and less than 0.1GPa when converted to a pressure). For the forces, the full diagonalisation results were 0.036 Ha/bohr for C, 0.016 Ha/bohr for Si and 0.014 Ha/bohr for Ge. The total energies were -47.891 Ha for C, -33.611 Ha for Si and -39.589 Ha for Ge.

The spatial decay of the density matrix is not analytically described for complex materials, but can be shown to decay approximately exponentially with gap[78–80]:

$$\rho(\mathbf{r}, \mathbf{r}') \propto \exp(-\gamma |\mathbf{r} - \mathbf{r}'|) \quad (17)$$

We can see in Fig. 9 that the rates of convergence of the different materials with density matrix truncation decrease with decreasing gap size, as expected. It is notable that the initial errors are largest for the stresses, and that significant differences in the stress remain even at very large density matrix ranges. We will investigate this fully in a future publication, but we are confident that this comes from the implicit dependence of energy on density matrix truncation range, which should be included in a stress calculation as it will change as the unit cell is changed; however, an analytic form for this stress is not available.

#### B. Structure optimisation

Structural optimisation can be performed using a variety of standard approaches: the L-BFGS algorithm for atomic optimisation; conjugate gradients for atomic and simulation cell optimisation; and quenched molecular dynamics (both in a simple form, and using the FIRE algorithm[81]). We note that some form of preconditioning will become increasingly important as system sizes increase, and we are planning to implement some recently proposed preconditioners[82, 83].

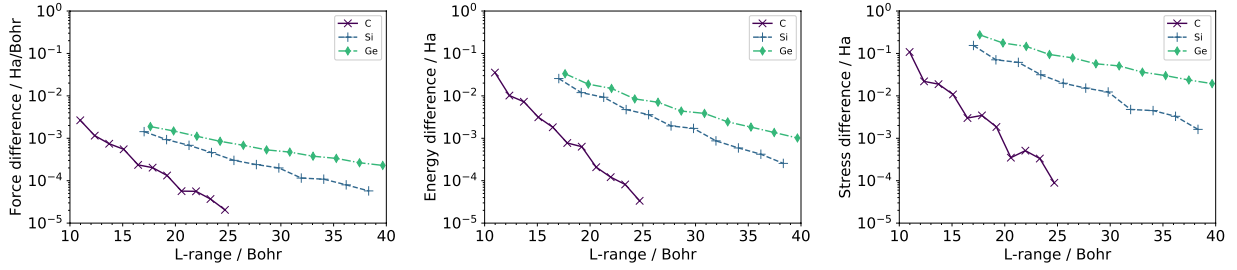


FIG. 9: Plots of difference between exact diagonalisation result and O(N) result for (a) force; (b) total energy; and (c) stress (not normalised by the simulation cell volume) for carbon (cross symbols), silicon (plus symbols) and germanium (diamond symbols).

### C. Molecular dynamics

Since the calculated forces are accurate and we can treat large systems, it is reasonable to expect that we can perform reliable molecular dynamics of large complex systems using CONQUEST. Unfortunately, it is not so easy to realize reliable MD simulations with the linear-scaling DFT technique, or with MSSF. We have two key issues here. First, the calculation time for each MD step should be small enough to reach a meaningful simulation time. Second, density matrix should be sufficiently accurate to produce reliable MD simulations. During structure optimization, we can refine the accuracy step by step, without significant penalty. In many cases, we need a rather high accuracy only in the late stages of structure optimization. On the other hand, for MD simulations, we need to calculate the density matrix accurately at every step to ensure that the correct trajectory is followed. The accuracy of the density matrix depends on the tolerance to which it is optimised. Here, the optimized quantities are the auxiliary density matrix  $L$  in the linear-scaling calculations and PAO coefficients of the support functions in the MSSF method. Hereafter, we focus the linear-scaling calculations.

For efficiency, we need a good initial guess of  $L$  matrix, at each MD step, and the simplest way, which should be efficient, is to use the  $L$  matrix optimized at the previous step. However, as is well known, this breaks the time-reversibility of the dynamics, resulting in a drift in the constant of motion over time[84]. Figure 10 shows the Born-Oppenheimer total energy ( $E_{BO}$ ), defined as the sum of the ionic kinetic energy  $T$  and the DFT total energy  $V_{BO}$ , for linear-scaling MD simulations of a 64-atom silicon crystalline system with different tolerances on the optimisation of the  $L$  matrix. The simulations are performed with the velocity-Verlet integrator with a time step of 0.5 fs in a microcanonical ( $NVE$ ) ensemble with initial velocities set so that the system temperature is 300K. The symbols in the figure show the time evolution of  $E_{BO}$ , which should be constant in reliable NVE-MD simulations. The results show that we need a very strict tolerance for stable MD simulations. Note that, if we use McWeeny initialization at every MD step (shown by solid

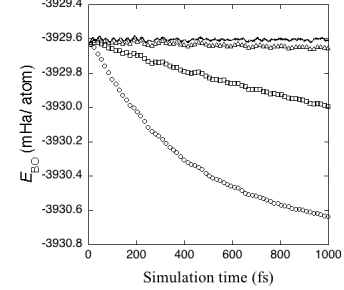


FIG. 10: Time evolution of Born-Oppenheimer total energy ( $E_{BO}$ ) obtained by McWeeny initialization at every step (solid line) and by reusing the  $L$  matrix from the previous step for different tolerances (symbols). Symbols indicate tolerances of  $1.6 \times 10^{-5}$  (circles),  $1.6 \times 10^{-7}$  (squares), and  $1.6 \times 10^{-9}$  (triangles). Reprinted with permission from J. Chem. Theor. Comput. 10, 5419 (2014). Copyright (2014) American Chemical Society.

line in Fig. 10),  $E_{BO}$  is almost constant even if we use a rough tolerance. But, this leads to a high computational cost at each iteration.

To solve this problem, CONQUEST uses the XLBOMD method[84–86], with the DMM method. The extended Lagrangian used in CONQUEST is[87]:

$$\mathcal{L}^{XBO}(\mathbf{X}, \dot{\mathbf{X}}, \mathbf{R}, \dot{\mathbf{R}}) = \mathcal{L}^{BO}(\mathbf{R}, \dot{\mathbf{R}}) + \frac{1}{2}\mu \text{Tr}[\dot{\mathbf{X}}^2] - \frac{1}{2}\mu\omega^2 \text{Tr}[(\mathbf{LS} - \mathbf{X})^2], \quad (18)$$

where  $\mathbf{S}$  is the overlap matrix and  $\mathbf{X}$  is a sparse matrix associated with  $\mathbf{LS}$  rather than  $\mathbf{L}$  to maintain the orthogonal metric.  $\mu$  is the fictitious electronic mass and  $\omega$  is the curvature of the electronic harmonic potential. If we take the limit  $\mu \rightarrow 0$ ,  $\mathcal{L}^{XBO}$  becomes  $\mathcal{L}^{BO}$  and we have equations of motion for nuclear positions and  $\mathbf{X}$ , and for  $\mathbf{X}$

$$\ddot{\mathbf{X}} = \omega^2(\mathbf{LS} - \mathbf{X}), \quad (19)$$

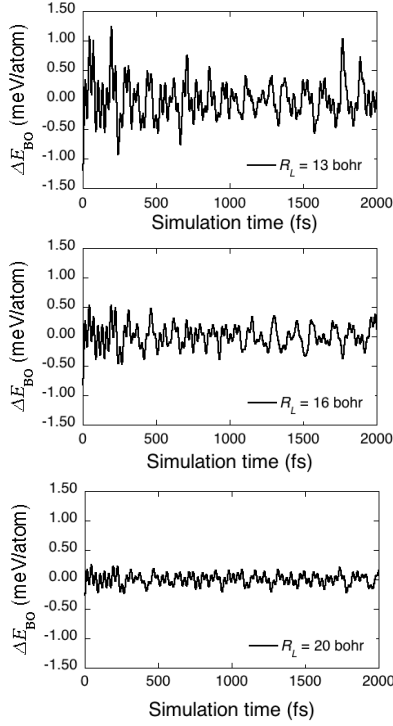


FIG. 11: Variation of  $E_{BO}$  during the *NVE* MD simulation of crystalline Si, with  $R_L = 13$  bohr (top), 16 bohr (middle), and 20 bohr (bottom). Reprinted with permission from J. Chem. Theor. Comput. 10, 5419 (2014). Copyright (2014) American Chemical Society.

If we apply the Verlet scheme to calculate  $\mathbf{X}$ , we have

$\mathbf{X}(t + \delta t) = 2\mathbf{X}(t) - \mathbf{X}(t - \delta t) + \delta t^2 \omega^2 [\mathbf{L}(t)\mathbf{S}(t) - \mathbf{X}(t)]$ , i.e. the trajectory of  $\mathbf{X}(t)$  is time-reversible, and evolves in a harmonic potential centred on the ground-state density  $\mathbf{L}(t)\mathbf{S}(t)$ . The matrix  $\mathbf{X}\mathbf{S}^{-1}$  is then used as the initial guess for the  $\mathbf{L}$ -matrix.

If we use this method, the total energy  $E_{BO}$  is stable and the MD trajectories do not strongly depend on the tolerance or the range  $R_L$  in the  $\mathcal{O}(N)$  calculations[87]. Figure 11 shows the variation of the total energy  $E_{BO}$  with simulation time for different values of  $R_L$ . The fluctuations in the energy are smaller for larger  $R_L$ , but even with  $R_L = 13$  bohr, the energy drift in  $E_{BO}$  is very small, meaning that the MD simulation is stable.

In practice, the  $\mathbf{X}$ -matrix sometimes moves away from the harmonic centre over time, increasing the number of SCF iterations required to reach the ground state over the course of a simulation. To remove this instability, the dissipative term,  $a \sum_{m=0}^M c_m \mathbf{X}(t - m\delta t)$ , is included[88]. In principle, this dissipation term may break the time-reversible symmetry, but it is made to have a minimal effect and it is found that the MD simulations with the term is stable.

Using this XLBOMD + DMM method, we can also treat the canonical ensemble and perform constant temperature (*NVT*) MD simulations, for example, using the

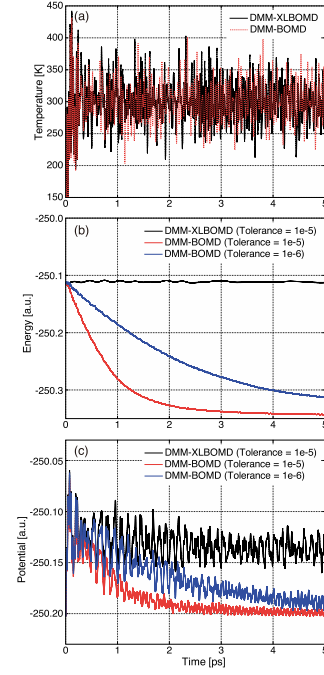


FIG. 12: Time evolution of the MD simulations of 64-atom Si crystalline systems in the canonical ensemble, for a) Temperature, b) constant of motion for the NHC method, and the potential energy ( $V_{BO}$ ). The results with XLBOMD method and those without using XLBOMD method, referred to as DMM-BOMD, are compared. Reproduced from Ref. 89 with permission. Copyright IOP Publishing. All rights reserved.

Nosé-Hoover chain (NHC) method[89]. The detailed explanation of the integration scheme used for the canonical ensemble is provided in Sec. A 2 a. Figure 12 shows the time evolution of the temperature, the constant of motion for the NHC method, and the DFT potential energy  $V_{BO}$ , in *NVT*-MD simulations of the same crystalline 64-atom silicon system at 300K, with and without XLBOMD method. We find that temperatures are stable and close to 300K in both simulations. However, we again observe the problem of drift in the constant of motion when we do not use the XLBOMD method, while there are no such problems in the XLBOMD+DMM simulations. More importantly, the profile of  $V_{BO}$  is completely different between the usual DMM and XLBOMD+DMM MD simulations. CONQUEST can also perform *NVT* simulations using the SVR (stochastic velocity rescaling) thermostat[90], which is extremely efficient and provides excellent conservation of the constant of motion, as described in Sec. A 2 d.

Since the stress tensors can be also calculated using CONQUEST with the DMM method, as shown in Sec. III A, it is also possible to include the degrees of freedom of the unit cell for *NPT* simulations with a given pressure, using the Parrinello-Rahman equations of motion[91]. CONQUEST uses the Martyna-Tobias-



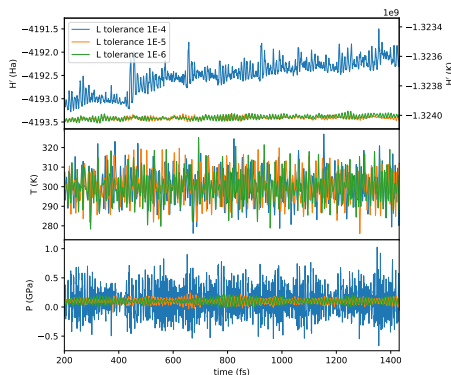


FIG. 13: NPT molecular dynamics on 1000 atom bulk silicon system. The three lines demonstrate the effect of varying the tolerance applied to the optimisation of the energy with respect to the density matrix during the  $\mathcal{O}(N)$  solution (“L-tolerance”).

Tuckerman-Klein modification[92], coupling the constant pressure equations of motion to a Nosé-Hoover chain thermostat to recover the NPT ensemble. The integration scheme used in the NPT ensemble is also explained in Sec. A 2 b.

This scheme is tested on a bulk crystalline silicon system containing 1,000 atoms, and the  $\mathcal{O}(N)$  method for finding the electronic ground state, as shown in Fig. 13. A minimal basis set (SZ) was employed, together with a grid cutoff of 100 Ha and the PBE exchange-correlation functional. The extended-Lagrangian scheme described above was used, with a velocity Verlet integrator for the  $X$  matrix and 5th order dissipation. The system was equilibrated using a Berendsen-type weak coupling thermostat and barostat, at a temperature of 300 K and pressure of 0.1 GPa. The cell volume was allowed to vary, but constrained to be cubic. An integration time step of 0.5 fs was used, with a 5th-order Yoshida-Suzuki integration scheme, and thermostat and barostat coupling time periods of 15 fs and 160 fs respectively. An *ad hoc* drag was applied to the barostat, reducing the velocities of the cell and its Nosé-Hoover thermostats by 5% each time-step. This was found to improve the stability, preventing the amplification of “ringing” of the barostat, with a minimal impact on energy conservation.

It can be seen that in order to achieve good energy conservation, the L-tolerance lower than  $10^{-5}$ , with a significant drift in the conserved quantity occurring at looser tolerances; without the XL-BOMD scheme, the tolerance required would be much tighter. We note that the NPT integrator is considerably more sensitive to the time step due to coupling between the thermostat and barostat degrees of freedom, and that in this case a time step of 1.0 fs also resulted in a significant energy drift, though we are seeking to alleviate this sensitivity.

## IV. PERFORMANCE

Here we demonstrate the performance of CONQUEST showing two examples, one for the MSSFs with diagonalisation and another for the  $\mathcal{O}(N)$  calculations.

### A. Performance of MSSF

A recent study on the graphene/Rh(111) interface [10] showcases both the accuracy and efficiency of the MSSFs. This study used large basis sets of PAOs contracted to a minimal size using the MSSF formalism, i.e., 15 and 22 PAOs of rhodium and carbon atoms are contracted to 6 and 4 MSSFs, respectively. In Ref. 10, it was demonstrated that the PAOs and MSSFs show comparable accuracy with plane-waves for the electronic and atomic structure of graphene/Rh(111), as shown in Fig. 14. The accuracy of PAOs has been further investigated in Ref. 24.

This study then demonstrates the great reduction in computational effort by using MSSFs. Table III shows the computational times of a SCF step for the graphene/Rh(111) systems consisting of 1544 and 3088 atoms (shown in Fig.15). MSSF clearly require more computational time for matrix construction than the PAOs, which comes from the calculations of the linear combination coefficients, as explained in Sec. II. On the other hand, the time to diagonalise the electronic Hamiltonian is reduced significantly by using MSSFs, because diagonalisation time scales cubically with the number of support functions. For the 1,544-atom system, the total time, i.e., the summation time of matrix construction and diagonalisation, is reduced by a factor of  $\approx 3$ , from 1,256.9 seconds to 439.6 seconds. For the 3,088-atom systems, when using 108 processes, the total time is reduced by a factor of  $\approx 18$ , from 37,803.5 seconds to 2,156.3 seconds, which indicates that the use of MSSFs becomes more efficient as systems become larger. Comparing the time for the matrix construction for the 1,544 atoms with 432 MPI processes and that for the 3,088 atoms with 864 MPI processes, i.e., when both the system size and the number of processes are doubled, the times are very close to each other, which indicates the construction of the MSSFs is  $\mathcal{O}(N)$  and parallelized ideally.

### B. Performance of $\mathcal{O}(N)$ calculations on massively parallel computers

The performance of CONQUEST on the Japanese, Fujitsu-made K-computer is of real significance [93]. This computer once topped the TOP500 list [94] (June and November 2011) and 8 years later *still featured* on the list in 20th place (November 2019) due to its impressive peak performance of 11,280.4 TFlops/s from its 705,024 physical cores. CONQUEST was found to display almost ideal parallel efficiency, as shown in Fig. 16c, utilising

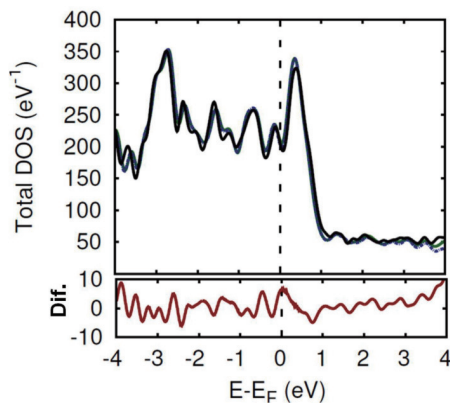


FIG. 14: Density of states of m14 graphene/Rh(111) calculated with plane-waves (black), PAOs (green) and MSSFs (blue). The red line in the lower panel represents the difference between the DOS calculated with PAOs and MSSFs. Reproduced from Ref. 10) with permission. Copyright IOP Publishing. All rights reserved.

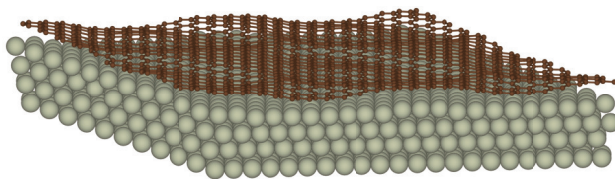


FIG. 15: Atomic structure of graphene/Rh(111) system (3,088 atoms).

	1544 atoms		3088 atoms		
	PAO	MSSF	PAO	MSSF	MSSF
No. of MPI process	432	432	108	108	864
Time [sec.]					
matrix construction	64.3	400.4	155.7	1455.4	405.9
diagonalisation	1192.5	39.2	37647.7	700.8	165.9
total <sup>a</sup>	1256.9	439.6	37803.5	2156.3	571.8

<sup>a</sup>Summation of matrix construction and diagonalisation.

TABLE III: Computational time for self-consistent-field calculation step with PAOs and MSSFs for graphene/Rh(111) performed on the supercomputer SGI ICE X in NIMS; data from Ref. 10.

up to 200,000 physical cores[93] on systems up to 2 million atoms [6]. (At present, there is no dynamic fault-tolerance built in to CONQUEST, to account for failure of nodes during a run; however, the frequency with which restart files are written can be controlled at a fine-grained level, which makes recovery from a crash easy.) Using crystalline silicon systems as a benchmark, it was demonstrated that in the  $\mathcal{O}(N)$  mode of operation that both strong scaling (the wall time for a fixed number of atoms, increasing the physical core count) and weak scaling (the wall time for a fixed number of atoms/physical core, increasing the number of atoms) performs very well. Specifically, for strong scaling it is found that performance is good should the number of atoms/core be  $\geq 4$  but for weak scaling, the performance is close to *per-*

*fect* for any given number of atoms per core all they way up to 2,000,000 atoms [6]. Strong scaling has also been tested on the UK national supercomputer ARCHER, a Cray XC30 MPP system (Figure 16a). This demonstrates also the high efficiency of the code until about 5 atoms/core. Going to fewer atoms/core than this starts to significantly impact the performance of CONQUEST; for this particular test, more than 50 atoms/core was feasible, but for more stringent tests, it would require large amounts of memory. When testing the scalability of the  $\mathcal{O}(N)$  algorithm itself (Figure 16b), we see that we achieve near-perfect linear scaling with system size even in the range of 2560-24565 atoms.

## V. APPLICATIONS

There are a multitude of physical systems to which CONQUEST has been applied. Studies using both exact diagonalisation (with and without the use of MSSFs) and the  $\mathcal{O}(N)$  mode of operation have all been exploited in large-scale structural relaxations and molecular dynamics. In the solid state, the code has been used to study the properties of nanowires [95, 96], Ge hut clusters on Si (001) surfaces [97], charge transport properties[98], interfaces between graphene with metals [10] and ferroelectric domain morphologies in perovskite oxide heterostructures. The code has also been applied to complex biological systems including hydrated DNA [99, 100] and gramicidin-A [101]. It is the purpose of this section to

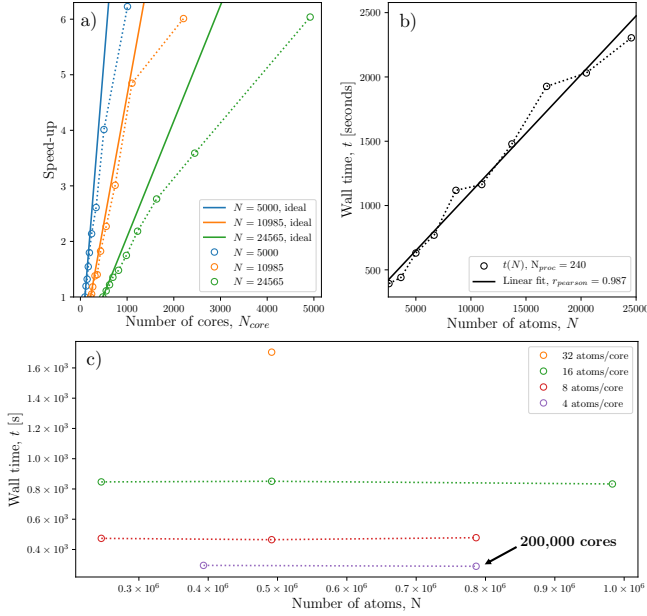


FIG. 16: Scaling performance for CONQUEST on the K-computer and ARCHER. (a) Strong scaling on the UK national supercomputer, ARCHER, up to 4,920 processors (from 50 atoms/core up to 5 atoms/core). Calculations are performed on bulk  $\text{PbTiO}_3$  with an  $L_{\text{range}}$  of  $14a_0$  and a SZ basis. (b) Demonstration of the scaling of the  $\mathcal{O}(N)$  algorithm on ARCHER for the same material system as (a). (c) Weak scaling on the K-computer up to 1,000,000 atoms for bulk Si.

outline some of these studies and to suggest areas that the code could find new applications.

### A. Nanoscale Ge/Si systems

One of the most important targets for large-scale DFT study is nano-structured semiconductors. Among them, Ge/Si systems have many attractive properties as a candidate for next-generation devices. Heteroepitaxy and strained growth in Ge/Si systems can be used as important techniques to control the structures and to explore new favorable properties.

CONQUEST was first applied to study the stability of Ge three-dimensional islands on Si substrate, called hut clusters, made of four equivalent Ge(105) facets. Experimentally, this 3D structure appears when the coverage of Ge atoms becomes large, after the formation of a two-dimensional (2D) structure with defects[102]. Here, CONQUEST calculations were performed with LDA and non-selfconsistent mode using a minimal basis set (SZ), whose accuracy were throughly investigated for Ge/Si systems[103]. The stability of the 3D structure in the heteroepitaxy systems is usually determined by the competition between the energy gain of the strain relief by the 3D structure and the energy loss due to the increase of the

surface area by the formation of facets in the 3D structures. However, the Ge/Si(001) system has the unique property that the strained Ge(105) facet is more stable than the strained Ge(001) surface[104, 105] even accounting for the increase in surface area. Thus, in order to clarify the stability of the 3D structure, it is necessary to include the effects of the edges between the facets and the finite area of the actual facets. For this, we need to treat the actual size of the hut clusters with a Si substrate. Standard DFT methods cannot treat the 3D structure with a size similar to experiments, but it is possible using CONQUEST with structure optimization. In the early study with CONQUEST, the total energies of systems having the same coverage of Ge atoms were compared between the 2D and 3D structures and it was found that the 3D structure becomes more stable when the coverage of Ge is larger than 2.7 monolayers[97]. This is close to the minimum coverage showing the transition from 2D to 3D growth in experiments, supporting the high accuracy of the present DFT method.

Further studies considered the stability of a single Ge dimer adsorbed at various sites on the facets[106]. This study aimed to clarify the initial process during the formation of a new facet layer. Experimentally, it has been reported that elongated hut clusters tend to grow, under certain growth conditions, by increasing the length of the longer side while keeping the width (shorter side) unchanged (See Fig. 17(a) [107]). The detailed mechanism underlying the growth of new facet layers is extremely difficult to obtain from experiments, since the complete facet is formed rapidly. We expect large-scale DFT calculations to play a significant role in clarifying these processes. By performing structure optimization for more than 100 different sites for the adsorption site of a single Ge dimer, as shown in Figure 17 (c), it was suggested that the top or the edges of the facets are the most preferable sites, and higher positions are more stable than lower ones. This kind of study is now possible with CONQUEST using a parallel supercomputer. The largest system in this study contains about 200,000 atoms, whose structure is shown in Fig. 17(b). Together with the study of double and triple dimer adsorptions, it was concluded that the new layer of facet is very likely to grow from top to bottom.

Recently, CONQUEST was also applied to study Si/Ge and Ge/Si core-shell nanowires, using SZP basis set with self-consistency. Semiconductor nanowires are promising candidates for the next-generation vertical-type transistors[109], and have been extensively studied both experimentally and theoretically. The core-shell type nanowires have many interesting and attractive properties[110–112] for next-generation electronics. All of these properties, however, will depend strongly on the size of core and shell. Using CONQUEST with the  $\mathcal{O}(N)$  method, strain distributions were calculated for nanowires with different sizes, shown in Fig. 18(a) up to experimentally accessible sizes. These are hexagonal Si/Ge core-shell nanowires along  $\langle 110 \rangle$  direction, and



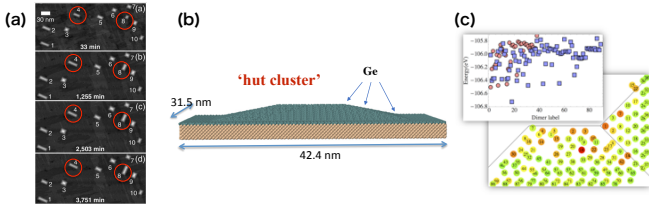


FIG. 17: Linear-scaling DFT study of Ge 3D structure on Si substrate using CONQUEST. (a) Experimental observation showing that Ge hut clusters grow, under certain conditions, by increasing the length of the longer side while keeping the width (shorter side) unchanged. (Reprinted from a figure[107] in Phys. Rev. Lett. 101, 216104 (2008) with permission. Copyright (2008) by the American Physical Society.) (b) The optimized structure of the largest structural model for Ge hut cluster on Si substrate, which contains about 200,000 atoms. (c) Adsorption energy map of single Ge dimers adsorbed on the  $\{105\}$  facets. Disks show the position of a given dimer on a facet projected on the  $x$ - $y$  plane. Dimers are labelled according to their height. Adsorption energy of dimers increases from red to green. top: Energy values of single Ge dimers on small (circles) and large (rectangles) facets. (Parts b and c reproduced from Ref. 108 with permission. Copyright IOP Publishing. All rights reserved.)

with numbers of atoms ranging from 612 to 2,404. The strain distributions in the core region of these nanowires are shown in Fig. 18(b). We can see that the strain is distributed anisotropically, depending on the direction of the bonds, and that large variations of strains exist in the interface and surface regions.

The structure of a more circular Si/Ge core-shell nanowire was also investigated and its band structure were calculated with the Sakurai-Sugiura (SS) method explained in Sec. IID, using the optimized structure and the self-consistent charge density obtained by  $\mathcal{O}(N)$  calculations. The occupied eigenstates near the Fermi level were also calculated and are shown in Fig. 18(c). We can clearly see that the distribution is anisotropic and localized in the Ge-shell region. The effect of arsenic doping and its dependence on the doping sites in the Si nanowires were also recently reported[96] using a rather high quality basis set (TZTP), with the MSSF method.

### B. $\text{PbTiO}_3$ films on $\text{SrTiO}_3$ substrates

Studies of the perovskite oxides can also make good use of large-scale electronic structure calculations. CONQUEST can be used to study large supercells of technologically relevant piezoelectric alloys like  $\text{PbZr}_x\text{Ti}_{1-x}\text{O}_3$ , where approximations designed to circumvent the need for large supercell calculations (like the virtual crystal approximation) are unable to quantify local structural

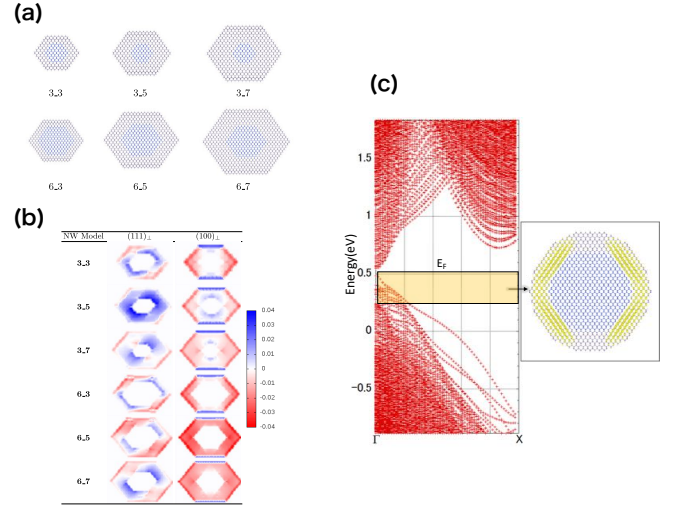


FIG. 18: (a) Structural models used in the study of Si/Ge nanowires along  $\langle 110 \rangle$  direction, labelled  $C_S$  where the index  $C$  represents the number of layers in the core and  $S$  the surface. Shell thickness increases left to right, and core thickness top to bottom. (b) Average bond strain map for the cross-section of the Ge shell of the SiGe-NWs. Maps for the bonds along different directions are shown, with extension illustrated in blue and compression in red. (c) Band structure of the circular Si/Ge core-shell nanowire and the charge density constructed from the occupied orbitals near the Fermi level (in the range shown in the band structure). (a) and (b) are reproduced from Ref. 95 with permission. (c) is reproduced from Ref. 108 with permission. All parts copyright IOP Publishing. All rights reserved.

distortions [113]. The study of ferroelectric domains in thin films is another problem requiring large-scale electronic structure calculations and *accurate* structural relaxations. Using the MSSF method and a large basis set of PAOs (DZDP), the nature of the ferroelectric flux closure domains in thin  $\text{PbTiO}_3$  films on  $\text{SrTiO}_3$  substrates was revealed. Using the initial geometry displayed in figure 19a, we were able to relax the system, to a stringent  $0.01 \text{ eV/\AA}$  force tolerance using quenched molecular dynamics. The force reduction for the first 50 steps is shown in figure 19b. Figure 19c shows the local polarisation vector field of a nine unit cell deep film. Such a field is calculated using the relaxed structure, the deviation in displacement from high symmetry sites and the Born effective charge tensors [114].

### C. Biological systems

Complex biological systems are one of the most important targets for large scale DFT simulations[14]. CONQUEST has been already applied to several biological sys-

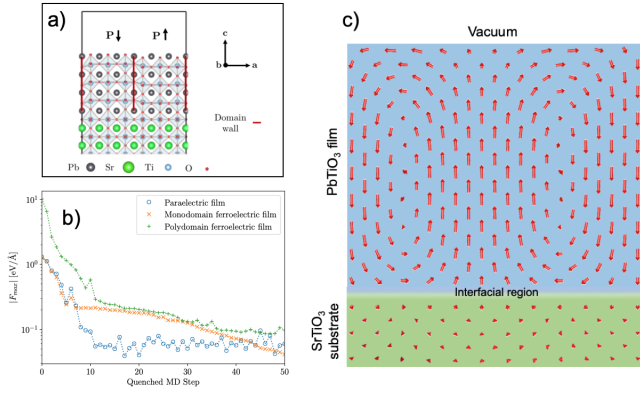


FIG. 19: The results of structural relaxation calculations with CONQUEST. (a) The initial geometry used to study ferroelectric flux closure domains in  $\text{PbTiO}_3$  films on  $\text{SrTiO}_3$  substrates. This example shows a three unit cell deep film with domain period of six unit cells. (b) The evolution the magnitude of maximum force on any atom for the first 50 quenched molecular dynamics steps for three different film configurations. (c) The local polarisation vector field of a 9 unit cell deep  $\text{PbTiO}_3$  film (2,088 atoms) on a  $\text{SrTiO}_3$  substrate.

tems, such as hydrated DNA[99, 100], dihydrofolate reductase (DHFR)[115], and the gramicidin A (gA) ion channel[101] systems. In the study of gA system, the optimized structure of the isolated gA molecule, shown in Fig. 20(b), was first calculated for the two previously reported structural models, 1MAG and 1JNO. The electronic structure of the gA molecule was also analyzed and it was concluded that the side chains of gA does not affect the electrostatic potential in the pore of gA. This kind of study of the isolated gA molecule cannot explain the selectivity of the ion permeation in the gA system, and it suggests the importance of simulating the system in the channel environment. We should treat the gA molecule in lipid bilayers sandwiched by bulk water regions, as is shown in Fig. 20(a). Using CONQUEST, we can perform stable self-consistent DFT calculations of such a complex system made of 17,102 atoms, having a rather irregular charge distribution. Figure 20(c) shows that the the density matrix minimization, for a SZP basis set, of this system is robust. It is important to note that, for stability in the self-consistency process, we need to update the charge density as well as the density matrix at each step in the calculation. More detailed information of this large-scale DFT study on the gA system will be reported in the future.

#### D. Large-scale MD simulations with Conquest

In Sec. V A, we introduced energetically stable structures of the perfect epitaxial models for Si/Ge core-shell

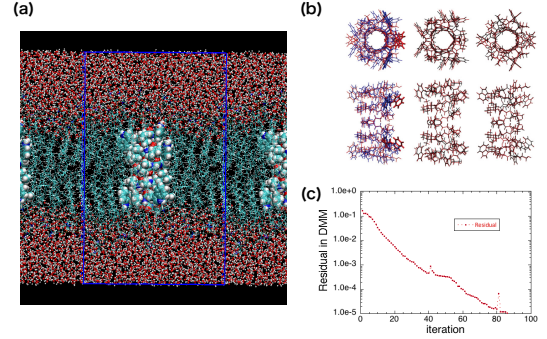


FIG. 20: (a) Structure model for the ion channel gramicidin A embedded in DMPC lipid bilayers, sandwiched with bulk water regions. (b) Left: Comparison of 1MAG (in blue) and 1JNO (in red) experimental structures. Middle and right: Optimized (red/light) and initial (black/dark) structures of isolated gA molecule starting from 1MAG (middle) or 1JNO (right) models. (c) Change of the residual during the density matrix minimization (DMM) step in the  $\mathcal{O}(N)$  calculations of the gA system shown in (a). In this calculation, the search direction in the minimization was reset at every 40 iterations. (a) and (b) are reproduced from Ref. 101 with permission.

nanowires. However, it is also important to investigate defects or Si-Ge intermixing at the interface for the actual nanowires. In addition, we sometimes need to clarify the thermodynamic stability or the dynamical processes. In such cases, molecular dynamics simulations based on DFT (DFT-MD) are useful and important. Using the XLBOMD + DMM method, explained in Sec. III(c), we are now able to do practical and reliable self-consistent DFT-MD simulations of very large systems. The MD simulations in this section used SZ (NWs,  $\text{SiO}_2$ ) and SZP (hydrated DNA) basis sets.

For perfect, epitaxial Si/Ge core-shell nanowires, DFT-MD simulations of nanowires containing 4,788 atoms, whose diameter is 10.4 nm (Si core is 7.2 nm and the thickness of Ge shell part is 1.6 nm), at 900K were recently performed. The DFT-MD simulations confirmed that the structure is stable at least up to 10 pico seconds. This does not guarantee that the perfect epitaxial model is more stable than other structures containing defects or intermixing, but it indicates that the model is at least a meta-stable structure. We also performed DFT-MD simulations of Si/Ge and Ge/Si core-shell nanowires at 3000K, whose snapshot structures are shown in Fig. 21(a) and (b). We observed that the Ge region melted first in both cases. As linear-scaling DFT-MD simulations on such large systems are now practical, we expect that

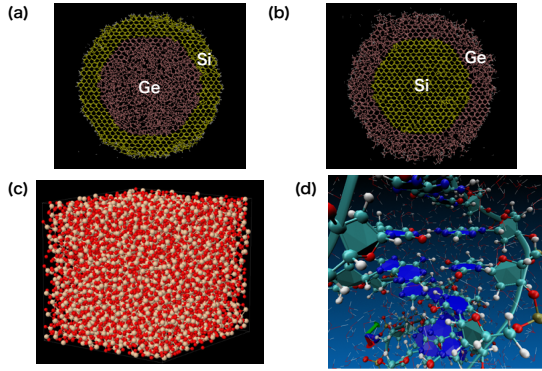


FIG. 21: Snapshot structures for (a) Ge/Si core-shell and (b) Si/Ge core-shell nanowires at 3000K, (c) melting SiO<sub>2</sub> at 3000K and 10GPa. (d) hydrated DNA system (details of the simulation are found in Ref.100).

they can be used to explore possible structures of various types of defects or intermixing effects at the Si/Ge interfaces by a local heating technique. Such study is now in progress. Furthermore, as we explained in Sec. III C, we can now perform DFT-MD simulations at a constant high temperature and a given high pressure. Structural properties of melting SiO<sub>2</sub> (Fig. 21(c)) are now being investigated using CONQUEST.

Of course, complex biomolecules, such as DNA in water, are also an important target for large-scale DFT-MD studies using CONQUEST, with a snapshot shown in Fig. 21(d). It is noteworthy that free energy calculations based on the blue moon ensemble method are now available with CONQUEST[116]. We expect a variety of dynamical processes or enzyme reactions in biological systems will be studied with CONQUEST in the future.

## VI. CONCLUSIONS

We have summarised the principles behind the implementation of the CONQUEST code, which enables it to address large scale DFT simulations, up to around 10,000 atoms with exact diagonalisation, and significantly larger systems, at least up to millions of atoms using linear scaling DFT. We showed how support functions can be represented in three ways, leading to a powerful approach for representing the density matrix. We also gave details on approaches to find the electronic structure of large systems, even with linear scaling, and indicated how hybrid DFT methods can be extended to extremely large systems.

We gave details of atomic movement, particularly molecular dynamics, and how the implementation and performance is affected by the use of linear scaling meth-

ods. We demonstrated that accurate, linear scaling MD is feasible with reasonable computational time, for standard ensembles (NVE, NVT and NPT, though care is needed with the calculation of stress and linear scaling). We then showed the performance of the MSSF approach, and how it opens up the possibility of exact diagonalisation simulations with many thousands of atoms. We also investigated the parallel performance of the code, both with MSSF and linear scaling, finding excellent performance including perfect scaling for certain approaches. We ended by giving examples of applications of the code, on systems with sizes ranging from hundreds of atoms to hundreds of thousands of atoms.

While large scale DFT calculations are challenging, in terms of the preparation of the system, the computing resources required, and the analysis of large data sets, it is clear that they are also now feasible for the majority of users. It is to be hoped that the size of most DFT calculations will grow from a few hundred atoms to many thousands, enabling greater accuracy, and new systems to be addressed.

## Acknowledgments

The authors would like to express their gratitude to all the developers and beta testers of CONQUEST who have contributed to the code over the years. In particular, Professor Mike Gillan initiated and oversaw the development and implementation for many years, and his input was invaluable. We also acknowledge, in alphabetical order, Michiaki Arita, Veronika Brazdova, Marius Buerkle, Rathin Choudhury, Chris Goringe, Eduardo Hernandez, Teruo Hirakawa, Chathurangi Kumarasinghe, Conn O'Rourke, Takao Otsuka, Alex Sena, Kane Shenton, Teppei Suzuki, Umberto Terranova, Milica Todorovic, Lianheng Tong, and Antonio Torralba.

This work was supported by World Premier International Research Centre Initiative (WPI Initiative) on Materials Nanoarchitectonics (MANA), Exploratory Challenge on Post-K computer by MEXT, and JSPS Grant-in-Aid for Scientific Research (18H01143, 17H05224, 15H01052). LT was supported by the BBSRC grant BB/H024217/1, "Linear Scaling Density Functional Theory for Biochemistry".

Calculations were performed on the Numerical Materials Simulator at NIMS, the supercomputer HA8000 system at Kyushu University, and by using the computational resources of the K computer provided by the RIKEN Advanced Institute for Computational Science through the HPCI System Research project (Project ID: hp160129, hp170264, hp180175, hp180226 and hp190096).

The authors are grateful for computational support from the UK Materials and Molecular Modelling Hub, which is partially funded by EPSRC (EP/P020194), for which access was obtained via the UKCP consortium and funded by EPSRC grant ref EP/P022561/1. They

also acknowledge computational support from the UK national high-performance computing service, ARCHER, for which access was obtained via the UKCP consortium and funded by EPSRC grant ref EP/K013564/1.

**Data availability** The data that support the findings of this study are available from the corresponding authors upon reasonable request.

- 
- [1] R. O. Jones, Rev. Mod. Phys. **87**, 897 (2015), URL <https://link.aps.org/doi/10.1103/RevModPhys.87.897>.
  - [2] J. M. Soler, E. Artacho, J. D. Gale, A. García, J. Junquera, P. Ordejón, and D. Sánchez-Portal, Journal of Physics: Condensed Matter **14**, 2745 (2002), ISSN 09538984, 0111138, URL <http://stacks.iop.org/0953-8984/14/i=11/a=302>.
  - [3] D. R. Bowler, T. Miyazaki, and M. J. Gillan, J. Phys.: Condens. Matter **14**, 2781 (2002).
  - [4] C.-K. Skylaris, P. D. Haynes, A. A. Mostofi, and M. C. Payne, J. Chem. Phys. **122**, 084119 (2005), URL <https://doi.org/10.1063/1.1839852>.
  - [5] M. J. Rayson and P. R. Briddon, Phys. Rev. B **80**, 205104 (2009).
  - [6] D. R. Bowler and T. Miyazaki, Journal of Physics: Condensed Matter **22**, 074207 (2010), URL <https://doi.org/10.1088/0953-8984/22/7/074207>.
  - [7] J. VandeVondele, U. Bortnik, and J. Hutter, J. Chem. Theory Comput. **8**, 3565 (2012), URL <https://doi.org/10.1021/ct200897x>.
  - [8] S. Mohr, L. E. Ratcliff, L. Genovese, D. Caliste, P. Boulanger, S. Goedecker, and T. Deutsch, Phys. Chem. Chem. Phys. **17**, 31360 (2015), URL <http://dx.doi.org/10.1039/C5CP00437C>.
  - [9] T. Ozaki, M. Fukuda, and G. Jiang, Phys. Rev. B **98**, 245137 (2018), URL <https://link.aps.org/doi/10.1103/PhysRevB.98.245137>.
  - [10] C. Romero-Muñiz, A. Nakata, P. Pou, D. R. Bowler, T. Miyazaki, and R. Pérez, Journal of Physics: Condensed Matter **30**, 505901 (2018), URL <https://doi.org/10.1088/1361-648x/aaec4c>.
  - [11] W. Kohn, Physical Review Letters **76**, 3168 (1996), URL <http://link.aps.org/doi/10.1103/PhysRevLett.76.3168>.
  - [12] S. Goedecker, Rev. Mod. Phys. **71**, 1085 (1999).
  - [13] D. R. Bowler and T. Miyazaki, Rep. Prog. Phys. **75**, 36503 (2012).
  - [14] D. J. Cole and N. D. M. Hine, Journal of Physics: Condensed Matter **28**, 393001 (2016), URL <https://doi.org/10.1088/2F0953-8984%2F28%2F39%2F393001>.
  - [15] D. R. Bowler, T. Miyazaki, A. Nakata, L. Truflandier, M. Arita, J. S. Baker, V. Brazdova, R. Choudhury, S. Y. Mujahed, J. T. Poulton, et al., *CONQUEST: Large-scale DFT calculations* (2020), <https://github.com/OrderN/CONQUEST-release>, URL <https://github.com/OrderN/CONQUEST-release>.
  - [16] D. R. Hamann, Phys. Rev. B **88**, 085117 (2013).
  - [17] D. Vanderbilt, Phys. Rev. B **32**, 8412 (1985).
  - [18] M. J. van Setten, M. Giantomassi, E. Bousquet, M. J. Verstraete, D. R. Hamann, X. Gonze, and G. M. Rignanese, Comp. Phys. Commun. **226**, 39 (2018).
  - [19] M. Schlipf and F. Gygi, Comp. Phys. Commun. **196**, 36 (2015).
  - [20] K. Lejaeghere, G. Bihlmayer, T. Bjrkman, P. Blaha, S. Blgel, V. Blum, D. Caliste, I. E. Castelli, S. J. Clark, A. Dal Corso, et al., Science **351**, aad3000 (2016).
  - [21] S. G. Louie, S. Froyen, and M. L. Cohen, Phys. Rev. B **26**, 1738 (1982), URL <https://link.aps.org/doi/10.1103/PhysRevB.26.1738>.
  - [22] O. F. Sankey and D. J. Niklewski, Phys. Rev. B **40**, 3979 (1989).
  - [23] T. Ozaki and H. Kino, Phys. Rev. B **72**, 045121 (2005).
  - [24] D. R. Bowler, J. S. Baker, J. T. L. Poulton, S. Y. Mujahed, J. Lin, S. Yadav, Z. Raza, and T. Miyazaki, Jap. J. Appl. Phys. **58**, 100503 (2019).
  - [25] E. Hernández, M. J. Gillan, and C. M. Goringe, Phys. Rev. B **53**, 7147 (1996).
  - [26] E. Hernández and M. J. Gillan, Phys. Rev. B **51**, 10157 (1995).
  - [27] E. Hernández, M. J. Gillan, and C. M. Goringe, Phys. Rev. B **55**, 13485 (1997).
  - [28] A. S. Torralba, M. Todorovic, V. Brázdová, R. Choudhury, T. Miyazaki, M. J. Gillan, and D. R. Bowler, J. Phys.:Condens. Matter **20**, 294206 (2008).
  - [29] A. Nakata, D. R. Bowler, and T. Miyazaki, J. Chem. Theory Comput. **10**, 4813 (2014), URL <http://dx.doi.org/10.1021/ct5004934>.
  - [30] A. Nakata, D. Bowler, and T. Miyazaki, Phys. Chem. Chem. Phys. **17**, 31427 (2015).
  - [31] M. Rayson, Comp. Phys. Commun. **181**, 1051 (2010).
  - [32] C. A. White, P. Maslen, M. S. Lee, and M. Head-Gordon, Chem. Phys. Lett. **276**, 133 (1997).
  - [33] M. S. Lee and M. Head-Gordon, J. Chem. Phys. **107**, 9085 (1997).
  - [34] G. Berghold, M. Parrinello, and J. Hutter, J. Chem. Phys. **116**, 1800 (2002).
  - [35] D. R. Bowler, I. J. Bush, and M. J. Gillan, Int. J. Quantum Chem. **77**, 831 (2000).
  - [36] N. D. Woods, M. C. Payne, and P. J. Hasnip, Journal of Physics: Condensed Matter **31**, 453001 (2019), URL <https://doi.org/10.1088%2F1361-648x%2F31c0>.
  - [37] P. Pulay, Chem. Phys. Lett. **73**, 393 (1980), ISSN 0009-2614, URL [http://dx.doi.org/10.1016/0009-2614\(80\)80396-4](http://dx.doi.org/10.1016/0009-2614(80)80396-4).
  - [38] L. S. Blackford, J. Choi, A. Cleary, E. D’Azevedo, J. Demmel, I. Dhillon, J. Dongarra, S. Hammarling, G. Henry, A. Petitet, et al., *ScaLAPACK Users’ Guide* (Society for Industrial and Applied Mathematics, Philadelphia, PA, 1997), ISBN 0-89871-397-8 (paperback).
  - [39] A. Marek, V. Blum, R. Johanni, V. Havu, B. Lang, T. Auckenthaler, A. Heinecke, H.-J. Bungartz, and H. Lederer, J. Phys.: Condens. Matter **26**, 213201 (2014).
  - [40] H. J. Monkhorst and J. D. Pack, Phys. Rev. B **13**, 5188 (1976).
  - [41] M. Methfessel and A. T. Paxton, Phys. Rev. B **40**, 3616 (1989), URL <http://dx.doi.org/10.1103/PhysRevB.40.3616>.



- 40.3616.
- [42] X.-P. Li, R. W. Nunes, and D. Vanderbilt, Phys. Rev. B **47**, 10891 (1993).
  - [43] R. W. Nunes and D. Vanderbilt, Phys. Rev. B **50**, 17611 (1994).
  - [44] A. H. R. Palser and D. E. Manolopoulos, Phys. Rev. B **58**, 12704 (1998).
  - [45] D. R. Bowler and M. J. Gillan, Comp. Phys. Commun. **120**, 95 (1999), URL [https://doi.org/10.1016/S0010-4655\(99\)00221-0](https://doi.org/10.1016/S0010-4655(99)00221-0).
  - [46] D. R. Bowler and M. J. Gillan, Comp. Phys. Commun. **112**, 103 (1998), URL [https://doi.org/10.1016/S0010-4655\(98\)00061-7](https://doi.org/10.1016/S0010-4655(98)00061-7).
  - [47] A. Nakata, Y. Futamura, T. Sakurai, D. R. Bowler, and T. Miyazaki, J. Chem. Theory Comput. **13**, 4146 (2017), URL <https://doi.org/10.1021/acs.jctc.7b00385>.
  - [48] T. Sakurai and H. Sugiura, J. Comput. Appl. Math. **159**, 119 (2003), URL [https://doi.org/10.1016/S0377-0427\(03\)00565-X](https://doi.org/10.1016/S0377-0427(03)00565-X).
  - [49] T. Sakurai, Y. Futamura, and H. Tadano, J. Algo. Comput. Tech. **7**, 249 (2013), URL <https://doi.org/10.1260/1748-3018.7.3.249>.
  - [50] I. Yamazaki, H. Tadano, T. Sakurai, and T. Ikegami, Parallel Computing **39**, 280 (2013).
  - [51] M. Toyoda and T. Ozaki, The Journal of Chemical Physics **130**, 124114 (2009), ISSN 0021-9606, 1089-7690, URL <http://aip.scitation.org/doi/10.1063/1.3082269>.
  - [52] M. Toyoda and T. Ozaki, Computer Physics Communications **181**, 1455 (2010), ISSN 00104655, URL <https://linkinghub.elsevier.com/retrieve/pii/S0010465510001141>.
  - [53] J. T. Fermann and E. F. Valeev, *Libint: Machine-generated library for efficient evaluation of molecular integrals over gaussians* (2003), freely available at <http://libint.valeev.net/> or one of the authors.
  - [54] H. Shang, Z. Li, and J. Yang, The Journal of Chemical Physics **135**, 034110 (2011), ISSN 0021-9606, 1089-7690, URL <http://aip.scitation.org/doi/10.1063/1.3610379>.
  - [55] X. Qin, H. Shang, H. Xiang, Z. Li, and J. Yang, Int. J. Quantum Chem. **115**, 647 (2015), ISSN 00207608, URL <http://doi.wiley.com/10.1002/qua.24837>.
  - [56] L. Truflandier, T. Miyazaki, and D. R. Bowler, *Linear-scaling implementation of exact exchange using localized numerical orbitals and contraction reduction integrals* (2012), arXiv:1112.5989v2.
  - [57] D. J. Wales and M. P. Hodges, Chemical Physics Letters **286**, 65 (1998), ISSN 0009-2614, URL <http://www.sciencedirect.com/science/article/pii/S0009261498000657>.
  - [58] A. Castro, A. Rubio, and M. J. Stott, Can. J. Phys. **81**, 1151 (2003), ISSN 0008-4204, URL <http://www.nrcresearchpress.com/doi/abs/10.1139/p03-078>.
  - [59] M. R. Jarvis, I. D. White, R. W. Godby, and M. C. Payne, Phys. Rev. B **56**, 14972 (1997), URL <http://link.aps.org/doi/10.1103/PhysRevB.56.14972>.
  - [60] G. J. Martyna and M. E. Tuckerman, J. Chem. Phys. **110**, 2810 (1999), URL <http://link.aip.org/link/JCPA6/v110/i6/p2810/s1&Agg=doi>.
  - [61] C. A. Rozzi, D. Varsano, A. Marini, E. K. U. Gross, and A. Rubio, Phys. Rev. B **73**, 205119 (2006), URL <http://link.aps.org/doi/10.1103/PhysRevB.73.205119>.
  - [62] I. Dabo, B. Kozinsky, N. E. Singh-Miller, and N. Marzari, Phys. Rev. B **77**, 115139 (2008), URL <http://link.aps.org/doi/10.1103/PhysRevB.77.115139>.
  - [63] H. Lee and M. E. Tuckerman, J. Chem. Phys. **129**, 224108 (2008), URL <http://link.aip.org/link/JCPA6/v129/i22/p224108/s1&Agg=doi>.
  - [64] M. A. Watson and K. Hirao, J. Chem. Phys. **129**, 184107 (2008), URL <http://link.aip.org/link/JCPA6/v129/i18/p184107/s1&Agg=doi>.
  - [65] K. Varga, Z. Zhang, and S. T. Pantelides, Phys. Rev. Lett. **93**, 176403 (2004), URL <http://link.aps.org/doi/10.1103/PhysRevLett.93.176403>.
  - [66] L. Genovese, T. Deutsch, A. Neelov, S. Goedecker, and G. Beylkin, J. Chem. Phys. **125**, 074105 (2006), URL <http://link.aip.org/link/JCPA6/v125/i7/p074105/s1&Agg=doi>.
  - [67] L. Genovese, T. Deutsch, and S. Goedecker, J. Chem. Phys. **127**, 054704 (2007), URL <http://link.aip.org/link/JCPA6/v127/i5/p054704/s1&Agg=doi>.
  - [68] G. Onida, L. Reining, R. W. Godby, R. Del Sole, and W. Andreoni, Phys. Rev. Lett. **75**, 818 (1995), URL <http://link.aps.org/doi/10.1103/PhysRevLett.75.818>.
  - [69] P. E. Blöchl, J. Chem. Phys. **103**, 7422 (1995), URL <http://link.aip.org/link/JCPA6/v103/i17/p7422/s1&Agg=doi>.
  - [70] P. A. Schultz, Phys. Rev. B **60**, 1551 (1999), URL <http://link.aps.org/doi/10.1103/PhysRevB.60.1551>.
  - [71] T. Miyazaki, D. R. Bowler, R. Choudhury, and M. J. Gillan, J. Chem. Phys. **121**, 6186 (2004).
  - [72] A. S. Torralba, D. R. Bowler, T. Miyazaki, and M. J. Gillan, J. Chem. Theory Comput. p. 1499 (2009).
  - [73] F. Knuth, C. Carbogno, V. Atalla, V. Blum, and M. Scheffler, Computer Physics Communications **190**, 33 (2015), URL <http://www.sciencedirect.com/science/article/pii/S0010465515000090>.
  - [74] O. H. Nielsen and R. M. Martin, Physical Review Letters **50**, 697 (1983), ISSN 00319007, URL <http://link.aps.org/doi/10.1103/PhysRevLett.50.697>.
  - [75] O. H. Nielsen and R. M. Martin, Physical Review B **32**, 3792 (1985), ISSN 0163-1829, URL <http://link.aps.org/doi/10.1103/PhysRevB.32.3792>.
  - [76] O. H. Nielsen and R. M. Martin, Physical Review B **32**, 3780 (1985), ISSN 01631829.
  - [77] O. H. Nielsen and R. M. Martin, Physical Review B **35**, 9308 (1987), ISSN 0163-1829.
  - [78] S. Ismail-Beigi and T. A. Arias, Physical Review Letters **82**, 2127 (1999), ISSN 10797114.
  - [79] L. He and D. Vanderbilt, Physical Review Letters **86**, 5341 (2001), ISSN 00319007.
  - [80] S. N. Taraskin, D. A. Drabold, and S. R. Elliott, Physical Review Letters **88**, 4 (2002), ISSN 10797114.
  - [81] E. Bitzek, P. Koskinen, F. Gähler, M. Moseler, and P. Gumbsch, Phys. Rev. Lett. **97**, 170201 (2006), URL <https://link.aps.org/doi/10.1103/PhysRevLett.97.170201>.
  - [82] D. Packwood, J. Kermode, L. Mones, N. Bernstein, J. Woolley, N. Gould, C. Ortner, and G. Csnyi, J. Chem. Phys. **144**, 164109 (2016), URL <https://doi.org/10.1063/1.4947024>.
  - [83] M. V. Fernández-Serra, E. Artacho, and J. M. Soler, Phys. Rev. B **67**, 100101 (2003), URL <https://link.aps.org/doi/10.1103/PhysRevB.67.100101>.
  - [84] A. M. N. Niklasson, Phys. Rev. Lett. **100**, 123004

- (2008), URL <http://link.aps.org/doi/10.1103/PhysRevLett.100.123004>.
- [85] A. M. N. Niklasson, C. J. Tymczak, and M. Challacombe, *Phys. Rev. Lett.* **97**, 123001 (2006).
- [86] A. M. N. Niklasson, *The Journal of Chemical Physics* **147**, 054103 (2017), URL <https://doi.org/10.1063/1.4985893>.
- [87] M. Arita, D. R. Bowler, and T. Miyazaki, *J. Chem. Theor. Comput.* **10**, 5419 (2014).
- [88] A. M. N. Niklasson, P. Steneteg, A. Odell, N. Bock, M. Challacombe, C. J. Tymczak, E. Holmström, G. Zheng, and V. Weber, *J. Chem. Phys.* **130**, 214109 (2009), URL <http://scitation.aip.org/content/aip/journal/jcp/130/21/10.1063/1.3148075>.
- [89] T. Hirakawa, T. Suzuki, D. R. Bowler, and T. Miyazaki, *J. Phys.: Condens. Matter* **29**, 405901 (2017).
- [90] G. Bussi, T. Zykova-Timan, and M. Parrinello, *J. Chem. Phys.* **130**, 074101 (2009).
- [91] M. Parrinello and A. Rahman, *J. Appl. Phys.* **52**, 7182 (1981).
- [92] G. J. Martyna, M. E. Tuckerman, D. J. Tobias, and M. L. Klein, *Mol. Phys.* **87**, 1117 (1996).
- [93] M. Arita, S. Arapan, D. R. Bowler, and T. Miyazaki, *Journal of Advanced Simulation in Science and Engineering* **1**, 87 (2014), URL <https://doi.org/10.15748/jasse.1.87>.
- [94] H. Meuer, E. Strohmaier, J. Dongarra, H. Simon, and M. Meuer, *Top 500 list* (2012).
- [95] C. O'Rourke, S. Y. Mujahed, C. Kumarasinghe, T. Miyazaki, and D. R. Bowler, *Journal of Physics: Condensed Matter* **30**, 465303 (2018), URL <https://doi.org/10.1088/1361-648x/aae617>.
- [96] C. Kumarasinghe and D. R. Bowler, *Journal of Physics: Condensed Matter* **32**, 035304 (2019), URL <https://doi.org/10.1088/1361-648x/ab4b3c>.
- [97] T. Miyazaki, D. R. Bowler, M. J. Gillan, and T. Ohno, *Journal of the Physical Society of Japan* **77**, 123706 (2008), URL <https://doi.org/10.1143/jpsj.77.123706>.
- [98] Y. Li, M. Buerkle, G. Li, A. Rostamian, H. Wang, Z. Wang, D. R. Bowler, T. Miyazaki, L. Xiang, Y. Asai, et al., *Nature Materials* **18**, 357 (2019), URL <https://doi.org/10.1038/s41563-018-0280-5>.
- [99] T. Otsuka, T. Miyazaki, T. Ohno, D. R. Bowler, and M. J. Gillan, *Journal of Physics: Condensed Matter* **20**, 294201 (2008), URL <https://doi.org/10.1088/0953-8984/20/29/294201>.
- [100] T. Otsuka, M. Taiji, D. R. Bowler, and T. Miyazaki, *Japanese Journal of Applied Physics* **55**, 1102B1 (2016), URL <https://doi.org/10.7567/jjap.55.1102b1>.
- [101] M. Todorović, D. R. Bowler, M. J. Gillan, and T. Miyazaki, *Journal of The Royal Society Interface* **10**, 20130547 (2013), URL <https://doi.org/10.1098/rsif.2013.0547>.
- [102] Y.-W. Mo, D. E. Savage, B. S. Swartzentruber, and M. G. Lagally, *Physical Review Letters* **65**, 1020 (1990), URL <https://doi.org/10.1103/physrevlett.65.1020>.
- [103] T. Miyazaki, D. R. Bowler, R. Choudhury, and M. J. Gillan, *Phys. Rev. B* **76**, 115327 (2007).
- [104] T. Hashimoto, Y. Morikawa, and K. Terakura, *Surf. Sci.* **576**, 61 (2005).
- [105] P. Raiteri, D. B. Migas, L. Miglio, A. Rastelli, and H. von Känel, *Phys. Rev. Lett.* **88**, 256103 (2002).
- [106] S. Arapan, D. R. Bowler, and T. Miyazaki, *A linear scaling dft study of the growth of a new 105 facet layer on a ge hut cluster*, arXiv:1510.00526 (2015).
- [107] M. R. McKay, J. A. Venables, and J. Drucker, *Phys. Rev. Lett.* **101**, 216104 (2008).
- [108] T. Miyazaki, *ECS Transactions* **86**, 269 (2018), URL <https://doi.org/10.1149/2F08607.0269ecst>.
- [109] C. Thelander, P. Agarwal, S. Brongersma, J. Eymery, L. F. Feiner, A. Forchel, M. Scheffler, W. Riess, B. J. Ohlsson, U. Gösele, et al., *Materials Today* **9**, 28 (2006), URL <http://www.sciencedirect.com/science/article/pii/S1369702106716510>.
- [110] W. Lu, J. Xiang, B. P. Timko, Y. Wu, and C. M. Lieber, *Proceedings of the National Academy of Sciences of the United States of America* **102**, 10046 (2005), URL <http://www.pnas.org/content/102/29/10046.abstract>.
- [111] J. Xiang, W. Lu, Y. Hu, Y. Wu, H. Yan, and C. M. Lieber, *Nature* **441**, 489 (2006), URL <https://doi.org/10.1038/nature04796>.
- [112] N. Fukata, M. Mitome, T. Sekiguchi, Y. Bando, M. Kirkham, J.-I. Hong, Z. L. Wang, and R. L. Snyder, *ACS Nano* **6**, 8887 (2012), URL <https://doi.org/10.1021/nn302881w>.
- [113] J. S. Baker and D. R. Bowler, *Physical Review B* **100** (2019), URL <https://doi.org/10.1103/physrevb.100.224305>.
- [114] B. Meyer and D. Vanderbilt, *Physical Review B* **65** (2002), URL <https://doi.org/10.1103/physrevb.65.104111>.
- [115] M. J. Gillan, D. R. Bowler, A. S. Torralba, and T. Miyazaki, *Computer Physics Communications* **177**, 14 (2007), URL <http://www.sciencedirect.com/science/article/pii/S0010465507001658>.
- [116] T. Hirakawa, D. R. Bowler, T. Miyazaki, Y. Morikawa, and L. A. Truflandier, arXiv **2003.01418** (2020), URL <https://arxiv.org/abs/2003.01418>.
- [117] S. Nos, *J. Chem. Phys.* **81**, 511 (1984).
- [118] W. G. Hoover, *Phys. Rev. A* **31**, 1695 (1985).
- [119] G. J. Martyna, M. L. Klein, and M. Tuckerman, *J. Chem. Phys.* **97**, 2635 (1992).
- [120] W. Shinoda, M. Shiga, and M. Mikami, *Phys. Rev. B* **69**, 4396 (2004).
- [121] G. Bussi, D. Donadio, and M. Parrinello, *J. Chem. Phys.* **126**, 014101 (2007).
- [122] H. J. C. Berendsen, J. P. M. Postma, W. F. van Gunsteren, A. Dinola, and J. R. Haak, *J. Chem. Phys.* **81**, 3684 (1984).
- [123] E. Hernández, M. J. Gillan, and C. M. Goringe, *Physical Review B* **53**, 7147 (1996), URL <http://link.aps.org/doi/10.1103/PhysRevB.53.7147>.
- [124] H. Shang, Z. Li, and J. Yang, *J. Phys. Chem. A* **114**, 1039 (2010), ISSN 1089-5639, 1520-5215, URL <https://pubs.acs.org/doi/10.1021/jp908836z>.
- [125] D. J. Cole and N. D. M. Hine, *Journal of Physics: Condensed Matter* **28**, 393001 (2016), URL <http://dx.doi.org/10.1088/0953-8984/28/39/393001>.
- [126] D. R. Bowler, J. S. Baker, J. T. L. Poulton, S. Y. Mujahed, J. Lin, S. Yadav, Z. Raza, and T. Miyazaki, *Japanese Journal of Applied Physics* **58**, 100503 (2019), URL <https://doi.org/10.7567/1347-4065/ab45af>.
- [127] We note that the overlap matrix can be inverted without problem when using exact diagonalisation.
- [128] As is common in the field, we use the term “exact diag-

onalisation” throughout the paper to indicate that the eigenstates and density matrix are found without search or approximation.

## Appendix A: Further details of MD implementation

Here, we explain the details of the integration scheme used in the molecular dynamics, since it is important for the actual implementation, and related to the stability of the molecular dynamics.

### 1. Microcanonical ensemble

The microcanonical ensemble is generated simply by solving Hamilton’s equation of motion for the Hamiltonian,

$$\mathcal{H} = \sum_{i=1}^N \frac{\mathbf{p}_i^2}{2m_i} + U(\mathbf{r}_i), \quad (\text{A1})$$

resulting in the following equations of motion:

$$\dot{\mathbf{r}}_i = \frac{\mathbf{p}_i}{m_i} \quad (\text{A2})$$

$$\dot{\mathbf{p}}_i = \frac{\partial U(\mathbf{r}_i)}{\partial \mathbf{r}_i} = \mathbf{F}_i \quad (\text{A3})$$

These equations are integrated using the velocity Verlet algorithm.

### 2. Non-Hamiltonian molecular dynamics

Hamiltonian dynamics describe systems that are isolated from their surroundings, and in order to generate the canonical and isobaric-isothermal ensembles, the system must be coupled to an external bath (heat for the former and heat and stress in the case of the latter). In the extended system approach, a set of *non-Hamiltonian* equations of motion including degrees of freedom for a thermostat and/or barostat are posited, and shown to generate the correct statistical ensemble *post hoc*.

#### a. Canonical (NVT) ensemble

The Nosé-Hoover Hamiltonian [117, 118] for the canonical ensemble can be written,

$$\mathcal{H} = \sum_i \frac{1}{2} m_i s^2 \dot{\mathbf{r}}_i^2 + U(\mathbf{r}_i) + \frac{1}{2} Q \dot{s}^2 - (n_f + 1) k_B T \ln s, \quad (\text{A4})$$

where  $\mathbf{r}_i$  and  $\dot{\mathbf{r}}_i$  are respectively the position and velocity of particle  $i$ ,  $U$  is the potential energy (in this case

the DFT total energy),  $s$  is a dimensionless quantity that can be interpreted *post hoc* as a time step scaling factor,  $Q$  is the fictitious mass of the heat bath and  $n_f$  is the number of ionic degrees of freedom. Hamilton’s equations of motion can then be solved to generate the Nosé-Hoover equations of motion. However, Martyna *et al.* demonstrate that this method does not generate an ergodic trajectory, and propose an alternative formulation with a chain of  $M$  coupled heat thermostats of mass  $Q_k$ , each with “position”  $\eta_k$  and conjugate momentum  $p_{\eta_k}$  [119], resulting in the following equations of motion.

$$\dot{\mathbf{r}}_i = \frac{\mathbf{p}_i}{m_i} \quad (\text{A5})$$

$$\dot{\mathbf{p}}_i = -\frac{\partial U(\mathbf{r})}{\partial \mathbf{r}_i} - \frac{p_{\eta_1}}{Q_1} \mathbf{p}_i \quad (\text{A6})$$

$$\dot{\eta}_k = \frac{p_{\eta_k}}{Q_k} \quad (\text{A7})$$

$$\dot{p}_{\eta_1} = \left( \sum_{i=1}^N \frac{\mathbf{p}_i^2}{m_i} - n_f k_B T \right) - \frac{p_{\eta_2}}{Q_{\eta_2}} p_{\eta_1} \quad (\text{A8})$$

$$\dot{p}_{\eta_k} = \left( \frac{p_{\eta_{k-1}}^2}{Q_{k-1}} - k_B T \right) - \frac{p_{\eta_{k+1}}}{Q_{k+1}} p_{\eta_k} \quad (\text{A9})$$

$$\dot{p}_{\eta_M} = \left( \frac{p_{\eta_{M-1}}^2}{Q_{M-1}} - k_B T \right) \quad (\text{A10})$$

These equations are integrated by constructing an appropriate Liouvillian and translated into an algorithm via the Trotter-Suzuki expansion, as described in Hirakawa *et al* [89].

#### b. Isobaric-isothermal (NPT) ensemble

The Parrinello-Rahman equations of motion [91] extend the constant volume equations of motion to include the degrees of freedom of the unit cell via the extended system approach. CONQUEST uses the Martyna-Tobias-Tuckerman-Klein modification [92], coupling the constant pressure equations of motion to a Nosé-Hoover chain thermostat to recover the NPT ensemble. For an cell unconstrained unit cell, the equations of motion are,

$$\dot{\mathbf{r}}_i = \frac{\mathbf{p}_i}{m_i} + \frac{\mathbf{p}_g}{W_g} \mathbf{r}_i \quad (\text{A11})$$

$$\dot{\mathbf{p}}_i = \mathbf{F}_i - \frac{\mathbf{p}_g}{W_g} \mathbf{p}_i - \left( \frac{1}{N_f} \right) \frac{\text{Tr}[\mathbf{p}_g]}{W_g} \mathbf{p}_i - \frac{p_\xi}{Q} \mathbf{p}_i \quad (\text{A12})$$

$$\dot{\mathbf{h}} = \frac{\mathbf{p}_g \mathbf{h}}{W_g} \quad (\text{A13})$$

$$\dot{\mathbf{p}}_g = V(\mathbf{P}_{\text{int}} - \mathbf{I}P_{\text{ext}}) + \left[ \frac{1}{N_f} \sum_{i=1}^N \frac{\mathbf{p}_i^2}{m_i} \right] \mathbf{I} - \frac{p_\xi}{Q} \mathbf{p}_g \quad (\text{A14})$$

$$\dot{\xi} = \frac{p_\xi}{Q} \quad (\text{A15})$$

$$\dot{\mathbf{p}}_g = \sum_{i=1}^N \frac{\mathbf{p}_i^2}{m_i} + \frac{1}{W_g} \text{Tr}[\mathbf{p}_g^T \mathbf{p}_g] - (N_f + d^2)kT, \quad (\text{A16})$$

where  $\mathbf{r}_i$ ,  $\mathbf{p}_i$  and  $m_i$  are respectively the position, momentum and mass of particle  $i$ ,  $\xi$ ,  $p_\xi$  and  $Q$  are the position, momentum and mass of the thermostat and  $\mathbf{h}$ ,  $\mathbf{p}_g$  and  $W_g$  are the matrix of lattice vectors, their velocities and the barostat mass. For simplicity, only a single Nosé-Hoover thermostat is included, but in CONQUEST a Nosé-Hoover chain is used. The Liouvillian is constructed, and the integrator constructed using the splitting of Shinoda *et al* [120],

$$iL = iL_r + iL_h + iL_v + iL_{\text{bath}}, \quad (\text{A17})$$

which can be further decomposed,

$$iL_{\text{bath}} = iL_{\text{box}} + iL_{\text{particles}} \quad (\text{A18})$$

$$iL_{\text{box}} = iL_{v_{\text{box}}} + iL_\xi + iL_{v_{\xi_1}} + iL_{v_{\xi_k}} + iL_{v_{\xi_M}} \quad (\text{A19})$$

$$iL_{\text{particles}} = iL_{v_{\text{part}}} + iL_\xi + iL_{v_{\xi_1}} + iL_{v_{\xi_k}} + iL_{v_{\xi_M}} \quad (\text{A20})$$

Then, using Liouville's theorem, we have,

$$iL_r = \sum_{i=1}^N [\mathbf{v}_i + \mathbf{v}_g \mathbf{r}_i] \cdot \nabla_{\mathbf{r}_i} \quad (\text{A21})$$

$$iL_h = \sum_{\alpha, \beta} \mathbf{v}_{g, \alpha \beta} \mathbf{h}_{\alpha \beta} \frac{\partial}{\partial \mathbf{h}_{\alpha \beta}} \quad (\text{A22})$$

$$iL_v = \sum_{i=1}^N \left( \frac{\mathbf{F}_i}{m_i} \right) \cdot \nabla_{\mathbf{v}_i} \quad (\text{A23})$$

$$iL_{\text{bath}} = iL_{v_{\text{part}}} + iL_{v_{\text{box}}} + iL_\xi + iL_{v_{\xi_1}} + iL_{v_{\xi_k}} + iL_{v_{\xi_M}} \quad (\text{A24})$$

$$\begin{aligned} &= \sum_{i=1}^N \left[ - \left\{ \mathbf{v}_g + \frac{1}{N_f} \text{Tr}(\mathbf{v}_g) + v_{\xi_1} \right\} \mathbf{v}_i \right] \cdot \nabla_{\mathbf{v}_i} \\ &+ \sum_{\alpha, \beta} \left[ \frac{F_{\text{box}}}{W} - v_{\xi_1} \mathbf{v}_{g, \alpha \beta} \right] \frac{\partial}{\partial \mathbf{v}_{g, \alpha \beta}} \\ &+ \sum_{k=1}^M v_{\xi_k} \frac{\partial}{\partial \xi_k} \\ &+ \left[ \frac{F_{\text{NHC}_1}}{Q_1} - v_{\xi_1} v_{\xi_2} \right] \frac{\partial}{\partial v_{\xi_1}} \\ &+ \sum_{k=2}^M \left[ \frac{1}{Q_k} (Q_{k-1} v_{\xi_{k-1}}^2 - kT_{\text{ext}}) - v_{\xi_k} v_{\xi_{k+1}} \right] \frac{\partial}{\partial v_{\xi_k}} \\ &+ \left[ \frac{1}{Q_M} (Q_{M-1} v_{\xi_{M-1}}^2 - kT_{\text{ext}}) \right] \frac{\partial}{\partial v_{\xi_M}}. \end{aligned}$$

In this instance, we use  $M$  Nosé-Hoover heat baths. The equations of motion can then be expanded via the Trotter-Suzuki identity, and directly translated into an algorithm.

$$e^{iL\Delta t} = e^{iL_{\text{bath}} \frac{\Delta t}{2}} e^{iL_v \frac{\Delta t}{2}} e^{iL_h \frac{\Delta t}{2}} e^{iL_r \Delta t} e^{iL_h \frac{\Delta t}{2}} e^{iL_v \frac{\Delta t}{2}} e^{iL_{\text{bath}} \frac{\Delta t}{2}}. \quad (\text{A25})$$

This integrator is tested on a bulk crystalline silicon system, as explained in Sec. III C.

### c. Weak-coupling thermostat and barostat

The Berendsen weak coupling method [122] involves global coupling to a pressure and/or heat bath via a Langevin-type equation of motion with a global friction constant. In the case of the thermostat, the ionic velocities are rescaled by a factor  $\lambda$ , which is scaled towards the target temperature  $T_0$  by the coupling frequency  $1/\tau_T$ .

$$\lambda = \left[ 1 + \frac{\Delta t}{\tau_T} \left( \frac{T_0}{T} - 1 \right) \right]^{\frac{1}{2}} \quad (\text{A26})$$

Similarly, for the barostat, the cell is rescaled by the matrix  $\mu$ , which is scaled towards a target pressure tensor  $\mathbf{P}_0$  by the pressure coupling frequency  $1/\tau_P$  and the estimated bulk modulus  $\beta$ .



$$\mu = \mathbf{I} - \frac{\beta \Delta t}{3\tau_P} (\mathbf{P}_0 - \mathbf{P}) \quad (\text{A27})$$

While trivial to implement, weak coupling will not generate the correct canonical or isobaric-isothermal velocity distribution, and the thermostat has the pathological effect of systematically transferring energy to the most slowly changing degrees of freedom (the “flying ice cube” effect). However, it may be useful for equilibration.

*d. Stochastic velocity rescaling*

Stochastic velocity rescaling [121] is essentially a modification of the weak coupling method that does not suffer from the flying ice cube effect. A correctly constructed random force is added to enforce the correct NVT (or NPT) phase space distribution. The kinetic energy is rescaled such that the change in kinetic energy between ionic steps is,

$$dK = (\bar{K} - K) \frac{dt}{\tau} + 2 \sqrt{\frac{K\bar{K}}{N_f}} \frac{dW}{\sqrt{\tau}}, \quad (\text{A28})$$

where  $\bar{K}$  is the target kinetic energy (i.e. heat bath temperature),  $dt$  is the time step,  $\tau$  is the time scale of the thermostat,  $N_f$  is the number of degrees of freedom and  $dW$  is a Wiener process. In practice, the particle velocities are rescaled by a factor  $\alpha$ , defined as,

$$\begin{aligned} \alpha^2 = & e^{-\Delta t/\tau} + \frac{\bar{K}}{N_f K} \left(1 - e^{-\Delta t/\tau}\right) \left(R_1^2 + \sum_{i=2}^{N_f} R_i^2\right) \\ & + 2e^{-\Delta t/2\tau} \sqrt{\frac{\bar{K}}{N_f K} \left(1 - e^{-\Delta t/\tau}\right)} R_1, \end{aligned} \quad (\text{A29})$$

where  $R_i$  is a set of  $N_f$  normally distributed random numbers with unitary variance. This thermostat can be used in NPT dynamics [90] by barostatting the system via the Parrinello-Rahman method, but with additional  $R_i$ ’s for the cell degrees of freedom, thermostating the cell velocities as well as the ionic velocities.